RSC Advances

PAPER

View Article Online
View Journal | View Issue



Cite this: *RSC Adv.*, 2021, **11**, 19333

# PEI functionalized $NaCeF_4:Tb^{3+}/Eu^{3+}$ for photoluminescence sensing of heavy metal ions and explosive aromatic nitro compounds†

Richa Singhaal, Lobzang Tashi, Zaib ul Nisa, Nargis Akhter Ashashi, Charanjeet Sen, Swaita Devi and Haq Nawaz Sheikh *

This work reports an eco-friendly hydrothermal approach for the synthesis of hexagonal $NaCeF_4:Tb^{3+}/Eu^{3+}$ nanophosphors. The phase, morphology and optical properties were characterized by Powder X-ray diffraction (PXRD), field emission scanning electron microscopy (FE-SEM), transmission electron microscopy (TEM), Fourier transform infrared (FT-IR) spectroscopy and photoluminescence (PL) spectroscopy respectively. Herein, the as-synthesized nanophosphor was functionalized with amine rich polyethylenimine (PEI) resulting in development of a luminescent nanoprobe bearing dual sensing functions for hazardous nitroaromatics and heavy metal ions. The strong photoluminescence emission of $Eu^{3+}$ ions was selectively quenched upon addition of toxic analytes at concentrations from 10 to 100 ppm due to complex formation between the analytes and PEI functionalized nanostructure. The synthesized nanomaterial shows sharp emission peaks at 493, 594, 624, 657 and 700 nm. Significantly, the peak at 594 nm shows a noticeable quenching effect on addition of toxic analytes to the aqueous solution of the nanocrystals. The nanophosphors are sensitive and efficient for the PA and $Fe^{3+}$ ion detection with an LOD of 1.32 ppm and 1.39 ppm. The Stern–Volmer (SV) quenching constant ($K_{SV}$) is found to be $2.25 \times 10^5$ $M^{-1}$ for PA and $3.8 \times 10^4$ $M^{-1}$ for $Fe^{3+}$ ions. The high $K_{SV}$ value and low LOD suggest high selectivity and sensitivity of the nanosensor towards PA and $Fe^{3+}$ ions over other analytes. Additionally, a reduced graphene oxide and nanophosphor based nanocomposite was also synthesized to investigate the role of energy transfer involving delocalized energy levels of reduced graphene oxide in regulating the luminescence properties of the nanophosphor. It was observed that PEI plays central role in inhibiting the quenching effect of reduced graphene oxide on the nanophosphor.

Received 14th April 2021
Accepted 12th May 2021

DOI: 10.1039/d1ra02910j

rsc.li/rsc-advances



## Introduction

Lanthanide doped luminescent nanomaterials have gained immense attention due to their potential applications in various fields such as drug delivery,[1] catalysis,[2] optoelectronics[3,4] and chemical sensing.[5] These nanocrystals are widely used for the identification of hazardous heavy metal ions (Fe, Cr, Co, Cd) and explosive aromatic nitro compounds (*p*-nitro aniline, picric acid, *p*-nitrophenol, 4-nitrotoulene).[6–8] The toxic chemical compounds are heavily spread over surface of soil *via* various anthropogenic activities like machinery and electronic manufacturing, fossil fuel, oil refining and electroplating.[9,10] The discharge of toxic chemical compounds into water disturb the whole ecosystem and has become a challenge worldwide. The pollution caused by chemical compounds originates from rapid industrial development and urbanization.[11] The release of the hazardous compounds into the environment has increased drastically in underdeveloped countries and may cause massive affect to all living creatures.[12,13] These chemicals can exert harmful effect on respiratory system, nervous system, connective – epithelial tissue, irritation to the eyes, inflammation in nose and skin.[14] The non-biodegradable nature of many chemical compounds in the environment deteriorates the situation than ever before.[15] A multipronged strategy is needed to tackle theses deleterious compounds. Researchers all around the world have employed various analytical techniques for the detection of heavy metal ions and aromatic nitro compounds like inductively coupled plasma mass spectrometry (ICPMS),[16] atomic absorption spectroscopy (AAS),[17] gas chromatography coupled with electron capture detection,[18] ion mobility spectroscopy (IMS),[19] Raman spectroscopy[20] and high-pressure liquid chromatography (HPLC).[21] However, these techniques are expensive and time-consuming since they depend on sophisticated equipment. These factors limit fast and convenient detection.

The metal ion ($Fe^{3+}$) is one of the most significant metal ions that play an important role in biological systems.[22] The $Fe^{3+}$ metal ion participates in many biological processes such as RNA

*Department of Chemistry, University of Jammu, Baba Sahib Ambedkar Road, Jammu-180006, India. E-mail: hnsheikh@rediffmail.com*

† Electronic supplementary information (ESI) available. See DOI: 10.1039/d1ra02910j

and DNA synthesis and helps in the oxygen transport capacity of haemoglobin. Deficiency and excess of this metal ion can cause serious disorders and diseases in human beings. The deficiency of $Fe^{3+}$ ions can lead to anaemia in the body, whereas its excess can cause life-threatening conditions, such as heart problems, liver and pancreas disease and diabetes.[23] Picric acid (PA) is also an essential chemical source used as an antiseptic agent for the ministration of burns, small pox, and malaria.[24] The PA continues to accumulate in the atmosphere as a highly toxic and poorly degradable compound, which poses pernicious influence to both the human (central nervous system and cardiovascular systems) and the environment.[25] Therefore, the detection of these toxic analytes becomes crucial for monitoring human health and the environment.

Lanthanide based photoluminescent nanocrystals have been proposed as potential material as new class of luminescent probes.[26] They exhibit exceptional chemical and optical properties particularly sharp emission peaks with large Stokes shift and longer lifetimes due to forbidden nature of intra 4f–4f transitions.[27–29] Moreover, the lanthanide-doped nanostructures shows a distinct set of sharp emission peaks independent of particle size compared to that of single and broad emission peaks observed for quantum dots or other nanoparticles.[30] Furthermore, the emission peak position is independent of the excitation wavelength.[31] The lanthanide-doped host matrix such as fluorides,[32] oxides,[33] phosphates[34] and oxysulfides[35] are thermally and photo-chemically stable.[36] The fluorides are appropriate among the hosts compared to other host matrices. This is due to their low phonon energies that can quickly reduce non-radiative relaxations, resulting in higher photoluminescence quantum yields.[37,38]

Malik and co-workers developed PEI functionalized $NaYF_4$:$Gd^{3+}/Tb^{3+}$ for selective detection of 2,4,6-trinitrotoluene *via* photoluminescent sensing technique. The PEI helps in detection of the hazardous nitroaromatic compound by the formation of the Meisenheimer complex and quenching the photoluminescence.[39] Tashi *et al.* fabricated down converting serine functionalized $NaGdF_4$:$Eu^{3+}/Ce^{3+}$@$NaGdF_4$:$Tb^{3+}$ core–shell nanomaterial for the selective and sensitive detection of picric acid.[40] Abbas and co-workers developed C-encapsulated three-dimensional Cu nano-pyramids (C@3DCu-PY) sensors for the control and monitoring of phenolic compounds.[41] Saleemi *et al.* reported a novel OVs rich spinel $ZnFe_2O_4$ micro-spheres (ZF-Ms) sensor for the effective detection of $As^{3+}$ metal ion present in underground water.[42] Abbas *et al.* fabricated a novel Cu nanoplates functionalized carbon nanoparticles (Cu@CNP) for the selective and sensitive detection of dopamine.[43]

Herein, we have synthesized PEI functionalized $NaCeF_4$:$Tb^{3+}/Eu^{3+}$ (see Scheme 1) for the selective detection of picric acid and $Fe^{3+}$ metal ion in the aqueous solution. The presence of PEI residues on the surface of synthesized nanocrystals hinders aggregation and increases water solubility of probe nanostructure. Moreover, acid–base reactivity of this luminescent probe facilitates effective binding of analytes on the surface of nanomaterial due to the formation of Meisenheimer complexes between electron-rich amine groups and electron deficient analytes.[44]

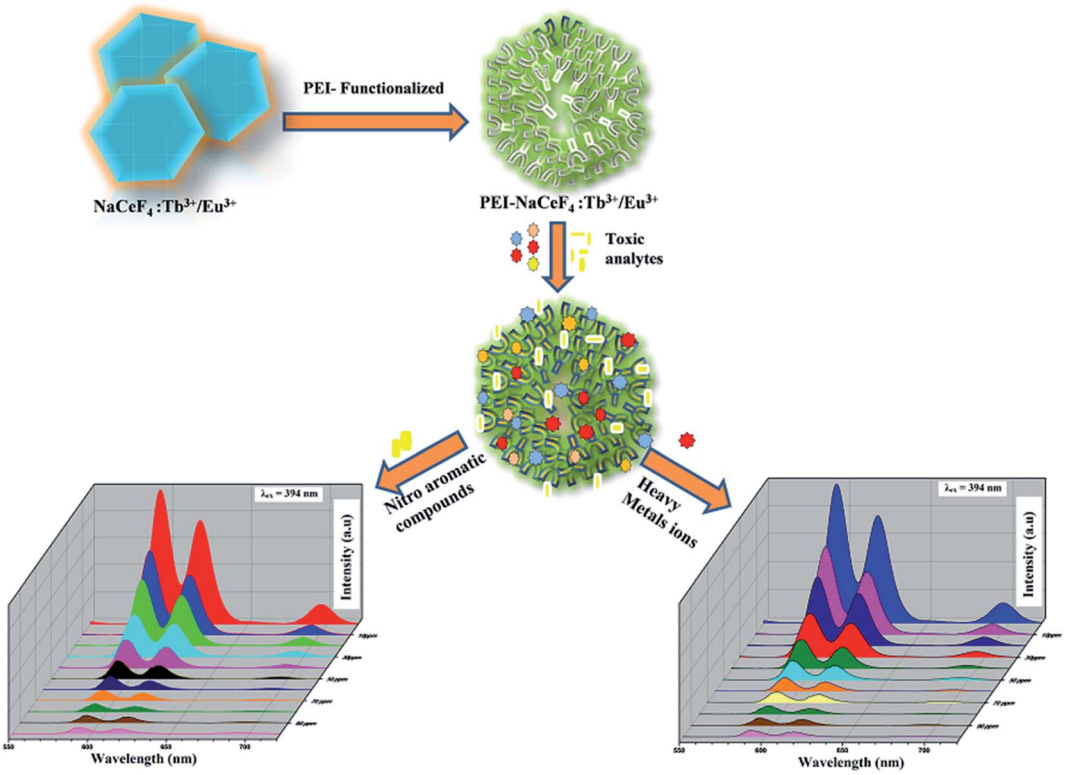


Scheme 1 Schematic procedure for the synthesis of $NaCeF_4$:$Tb^{3+}/Eu^{3+}$ (Eu-7%) and PEI functionalized $NaCeF_4$:$Tb^{3+}/Eu^{3+}$ (Eu-7%) nanophosphors.

Additionally, to unravel the effect of graphene derivatives on the photoluminescence properties of the nanophosphor, R-GO@PEI-$NaCeF_4$:$Tb^{3+}$/$Eu^{3+}$ nanocomposite was synthesized with and without the functionalizing material. The results showed a remarkable improvement in the PL intensity resulting in the red emission of nanocomposite with the addition of the amine rich PEI ligand rather than without the PEI attached nanocomposite.

## Experimental section

### Chemicals and materials

All the chemicals used in the work including terbium(III) nitrate hexahydrate Tb $(NO_3)_3 \cdot 6H_2O$ (99.9%), cerium(III) nitrate hexahydrate Ce $(NO_3)_3 \cdot 6H_2O$ (99.5%), europium(III) nitrate hexahydrate Eu $(NO_3)_3 \cdot 6H_2O$ (99.7%), ammonium tetrafluoroborate $NH_4BF_4$ and ethylenediaminetetraacetic acid (EDTA) were purchased from Alfa Aesar. Nitric acid ($HNO_3$), phosphoric acid ($H_3PO_4$), potassium permanganate $KMnO_4$ and ethanol all were of analytical grade. Graphite flakes and polyethylenimine (PEI) were procured from Sigma Aldrich. All the chemicals were used without further purification. Tripled time distilled water was used for experiments.

### Synthesis of $NaCeF_4$:$Tb^{3+}$ nanophosphors

In a usual procedure, a series of Tb doped $NaCeF_4$ phosphors were fabricated *via* modified hydrothermal method at varying temperature conditions. In a typical synthesis method Tb $(NO_3)_3 \cdot 6H_2O$ (0.05 mmol, 0.0217 g), Ce $(NO_3)_3 \cdot 6H_2O$ (0.95 mmol, 0.4125 g) were dissolved in 10 mL of distilled water and further stirred for 10 minutes for proper mixing of both the metal ions. Separately, 0.37 g (1 mmol) of $Na_2EDTA$ was added to 5 mL of distilled water and stirred for 15 minutes. After continuous stirring, the two solutions were mixed together and agitated for half an hour at room temperature. To the resultant reaction mixture, 5 mL aqueous solution of NaOH was drop wise added under continuous stirring followed by addition of 10 mL of ethanol. Lastly, 2 mL aqueous solution of $NH_4BF_4$ (6 mmol, 0.629 g) was drop wise added into the reaction solution followed by vigorous stirring for 1 hour at room temperature. The resultant precursor solution was finally transferred into a 50 mL Teflon-lined autoclave and heated at 120 °C for 24 h. The reaction vessel was naturally cooled down at room temperature. The obtained product was separated by centrifugation and repeatedly washed with distilled water followed by 10% ethanol. The product obtained was finally dried at 70–80 °C for 12 h. Three more samples with the same chemical composition were synthesized under similar experimental conditions, at varying temperatures (140 °C, 160 °C, and 180 °C) for 24 h.

### Synthesis of $NaCeF_4$:$Tb^{3+}$ co-doped $Eu^{3+}$

In a similar procedure, $NaCeF_4$:$Tb^{3+}$ co-doped $Eu^{3+}$ nanostructures were synthesized with 5% $Tb^{3+}$ doping and with varying $Eu^{3+}$ ion concentrations (1%, 3%, 5%, 7%). $Na_2EDTA$ was chosen as surfactant or surface directing agent for better morphology of the nanoparticles. Tb $(NO_3)_3 \cdot 6H_2O$ (0.05 mmol, 0.0217 g), $Ce(NO_3)_3 \cdot 6H_2O$ (0.94 mmol, 0.408 g) and $Eu(NO_3)_3 \cdot 6H_2O$ (0.01 mmol, 0.004 g) were dispersed in 7 mL of distilled water and stirred for about 10 minutes until complete dissolution. 0.37 g (1 mmol) of $Na_2EDTA$ was added to 7 mL of distilled water and stirred for further 10 minutes. The two solutions were then mixed together and continuously stirred for extra 30 minutes. Additionally, 5 mL aqueous solution of NaOH was added drop wise followed by 10 mL of ethanol and 2 mL solution of $NH_4BF_4$ (6 mmol, 0.629 g) under vigorous stirring for 1.5 h at room temperature. The resultant reaction mixture was then transferred into a 50 mL Teflon-lined autoclave and the reaction vessel was heated at 160 °C for 24 h. The reaction vessel was cooled down naturally and the product so obtained was centrifuged and washed three times with distilled water followed by ethanol. The product was finally dried at 60 °C for 24 h.

Under similar experimental conditions, three more samples were synthesized at same temperature conditions like (160 °C at 24 h) but different Eu ion concentrations (3%, 5% and 7%).

### PEI-surface functionalization of nanophosphor

In a typical hydrothermal method, 0.01 g of as synthesized $NaCeF_4$:$Tb^{3+}$/$Eu^{3+}$ (Eu-7%) sample was dispersed in a 10 mL of water and sonicated for 30 minutes. Furthermore, 0.02 g of PEI was separately mixed in 10 mL of water and sonicated for about 15 minutes until proper mixing. Finally, dropwise PEI solution was added to the above sonicated solution with further addition of 5 mL ethanol followed by vigorous stirring for about 1 h. The surface-functionalized nanomaterial PEI @$NaCeF_4$:$Tb^{3+}$/$Eu^{3+}$ (Eu-7%) so obtained was separated by centrifugation, washed twice with distilled water followed by ethanol washing and finally vacuum dried at room temperature for 24 h.

### Synthesis of graphene oxide (GO)

Graphene oxide (GO) was prepared by one-pot synthesis gleaned from new improved Hummers method.[45] Natural graphite flakes were used as the precursor material and $KMnO_4$ as the oxidising agent for the preparation of GO. In a typical procedure, 1 g of pure graphite flakes were dissolved in a solution containing stichometric ratio 9 : 1 of sulphuric acid and phosphoric acid and vigorously stirred for about 6 h. The suspension mixture was then kept in an ice bath and the temperature was adjusted below 5 °C. Next, 8 g of $KMnO_4$ was added slowly into the mixture while stirring followed by stirring for 1.5 h. The resulting green color suspension was further stirred in a water bath (40 °C) for 2 h. The mixture was then adjusted to a linearly high temperature of 70 °C and stirred for about 45 minutes. Later, distilled water was added to the brown color suspension mixture and then transferred into beaker containing 400 mL of additional water. In order to terminate the oxidation process 15 mL of $H_2O_2$ was added and mixed vigorously for 10 minutes imparting yellow color. The product obtained was finally separated by centrifugation and then repeatedly decant off with distilled water followed by 10% HCl solution. Lastly, the solid product was dried under vacuum at room temperature and product was obtained as GO powder. Additionally, the reduced graphene oxide (R-GO) was synthesized by simple hydrothermal method using hydrazine hydrate and ammonia as the reducing agent as described in the literature.[46]

### Synthesis of R-GO@PEI@$NaCeF_4$:$Tb^{3+}$/$Eu^{3+}$

A facile hydrothermal route was used for the synthesis of nanocomposite material. 0.02 g of R-GO was dispersed in 15 mL distilled water and sonicated for 40 minutes. Separately, 0.08 g of as-synthesized PEI-functionalized $NaCeF_4$:$Tb^{3+}$/$Eu^{3+}$ (Eu-7%) nanomaterial was dispersed in 30 mL of distilled water and sonicated for 20 minutes. The two solutions were mixed together followed by addition of 7 mL ethanol and stirred for 1 h. Finally, the suspension mixture was centrifuged and washed twice with distilled water followed by 10% HCl solution. The solid product was vacuum dried at room temperature for 24 h.

### Spectroscopic and microscopic measurement

X-Ray diffraction (XRD) data was used to determine the phase purity and crystallite size of as-synthesized nanophosphors. The XRD data was collected using D8 X-ray diffractometer (Bruker) at scanning rate of 12 $min^{-1}$ in the $2\theta$ range of 10 to 80° with Cu K$\alpha$ radiation ($\lambda$ = 0.15405 nm). Field emission scanning electron micrographs (FE-SEM) were recorded on FEI Nova Nano SEM-450 to examine the external morphology and particles size of as-synthesized nanophosphors. The internal composition, lattice parameters, grain size and morphology was recorded by using transmission electron microscopy (TEM) and high-resolution TEM (HR-TEM). The high-resolution TEM (HR-TEM) was recorded on Tecnai G2 S-Twin transmission electron microscope having field emission gun operating at 200 kV. The presence of surface directing agent as well as the functionalized materials which was assimilated on the surface of nanocrystals was explored by Shimadzu Fourier Transform Infrared Spectrophotometer (FT-IR) using standard KBr pellet technique (4000–400 $cm^{-1}$). For UV-visible down conversion photoluminescence emission spectra of as-synthesized nanophosphors Hitachi F-4700 Fluorescence Spectrophotometer having xenon lamp as excitation source was employed.

### Sensing of hazardous nitroaromatics and heavy metal ions

The Photoluminescence detection experiment for the sensing of heavy metal ions and explosive aromatic nitro compounds were carried out on Hitachi F-4700 Fluorescence Spectrophotometer at room temperature. PEI-functionalized $NaCeF_4$:$Tb^{3+}$/$Eu^{3+}$ nanostructure (0.03 g) was dispersed in 30 mL of distilled water and sonicated for around 20 minutes. Six stock solutions of explosives were prepared by dissolving 0.1 g of each of nitro-aromatic compounds as well as heavy metal ions in 100 mL of water (1000 ppm solution). From the stock solutions, ten different solutions of each compound were prepared by simple dilution having concentrations ranging from 10–100 ppm. To each dilute solution, 2 mL of as prepared sample suspension was added. The florescence spectrum of each solution was recorded immediately. Herein, for sensing of nitro-compounds as well as heavy metals ions the luminescence spectra was analyzed by exciting the PEI-functionalized $NaCeF_4$:$Tb^{3+}$/$Eu^{3+}$ luminescent material selectively at 394 nm for the solution phase at variant ppm concentrations.

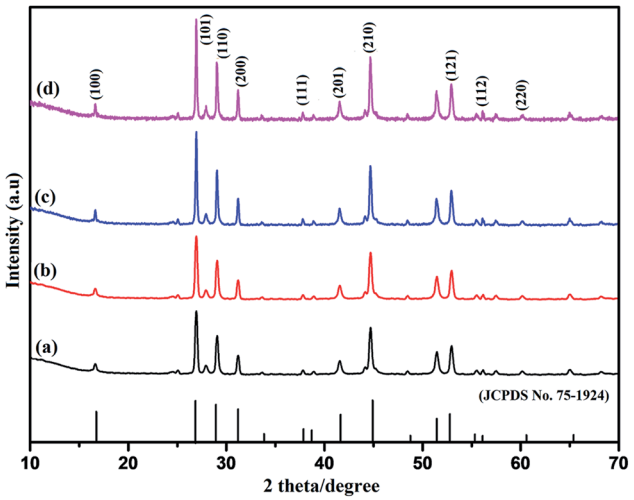


Fig. 1 PXRD patterns of as-synthesized $NaCeF_4$:$Tb^{3+}$/$Eu^{3+}$ (*x*%) nanoparticles with different $Eu^{3+}$ ion concentrations: (where *x* = (a) 1% (b) 3% (c) 5% (d) 7%).

## Result and discussion

### Powder X-ray diffraction

The composition, phase evolution, purity, and size of the as-prepared sodium cerium fluoride core doped with rare earth metals ions were confirmed by PXRD technique. A series of $NaCeF_4$:$Tb^{3+}$ nanocrystals samples were synthesized keeping the reaction time and concentration of the metals ions as well as the concentration of the surfactant (EDTA) constant while varying the reaction temperature. Fig S1: ESI† shows the diffraction pattern of synthesized $NaCeF_4$:$Tb^{3+}$ nanophosphors at different heating temperatures. All the diffraction peaks are in good agreement with the JCPDS no. 75-1924.[47] Furthermore, to explore the effect of doping ions concentration on the structure of nanophosphors, another series of $NaCeF_4$:$Tb^{3+}$/$Eu^{3+}$ nanocrystals with different $Eu^{3+}$ ion concentration were

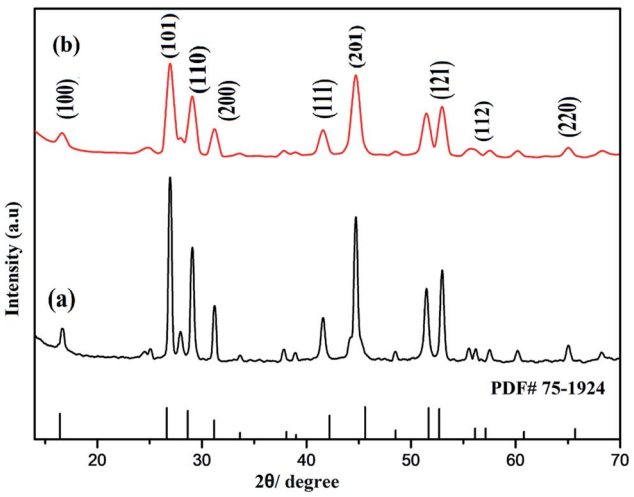


Fig. 2 Comparison of PXRD patterns of prepared nanostructures: (a) $NaCeF_4$:$Tb^{3+}$/$Eu^{3+}$ (Eu-7%) (b) PEI@ $NaCeF_4$:$Tb^{3+}$/$Eu^{3+}$ (Eu-7%).

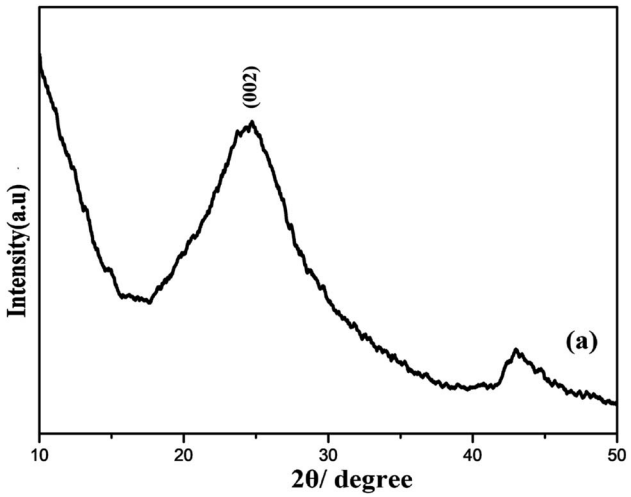


Fig. 3 PXRD pattern of (a) R-GO.

prepared keeping the reaction time, temperature and molar concentration of surfactant constant. Fig. 1 shows the diffraction pattern of the as-synthesized nanophosphors. It was observed that all the diffraction peaks of nanocrystals are in accordance with the JCPDS no. 75-1924 and are perfectly indexed to pure hexagonal phase. From the XRD pattern (Fig. 1), the $Eu^{3+}$ concentrations do not cause any difference in the crystal phase and structure of nanophosphors. All the diffraction peaks can be readily indexed as the hexagonal $NaCeF_4$, agreeing well with the data reported in the JCPDS no. 75-1924.[48] However, only small variation in particles size can be seen. The powder XRD patterns of as-synthesized nanocrystals were systematically investigated and no extra impurity peak was observed clearly indicating that $Tb^{3+}$ and $Eu^{3+}$ ions were perfectly dissolved in the $NaCeF_4$ host lattice without further alteration in the crystal structure.

It was also observed that no additional peak was noticed in the spectra of nanophosphors with amine rich ligand (polyethylenimine (PEI)). However the diffraction pattern gets broadened which signify the nanoscale range of as-synthesized nanocrystals as shown in Fig. 2.

Scherrer's eqn (1) was applied to calculate the crystallite sizes of the as-synthesized nanomaterial:[49]

$$L = \frac{K\lambda}{\beta \cos \theta} \quad (1)$$

Here, $L$ (nm) is the crystallite size, $K$ is the Scherrer constant (equals to 0.89), $\lambda$ (nm) is the wavelength of the Cu K$\alpha$ radiant, $\lambda =$ 0.15405 nm, $2\theta$ is the diffraction angle, $\beta$ is the full-width at half-maximum (FWHM) of the diffraction peak. The average crystallite size was calculated by using the major diffraction peaks of nanocrystals. The average crystallite size of $NaCeF_4$:$Tb^{3+}$/$Eu^{3+}$ for nanostructures were observed in the range of 15 to 21 nm.

Furthermore, the XRD pattern of R-GO was systematically examined. A strong characteristics peak centered at $2\theta = 23°$ corresponding to (002) plane and additional small peak around $2\theta = 45°$ were observed as shown the Fig. 3. The presence of wide peak width clearly demonstrates the small crystallite size and short layered stacked structure of R-GO.[50]

### Energy dispersive X-ray spectroscopic analysis

The energy dispersive X-ray spectroscopy (EDS) analysis was used to determine the exact elemental content in the prepared

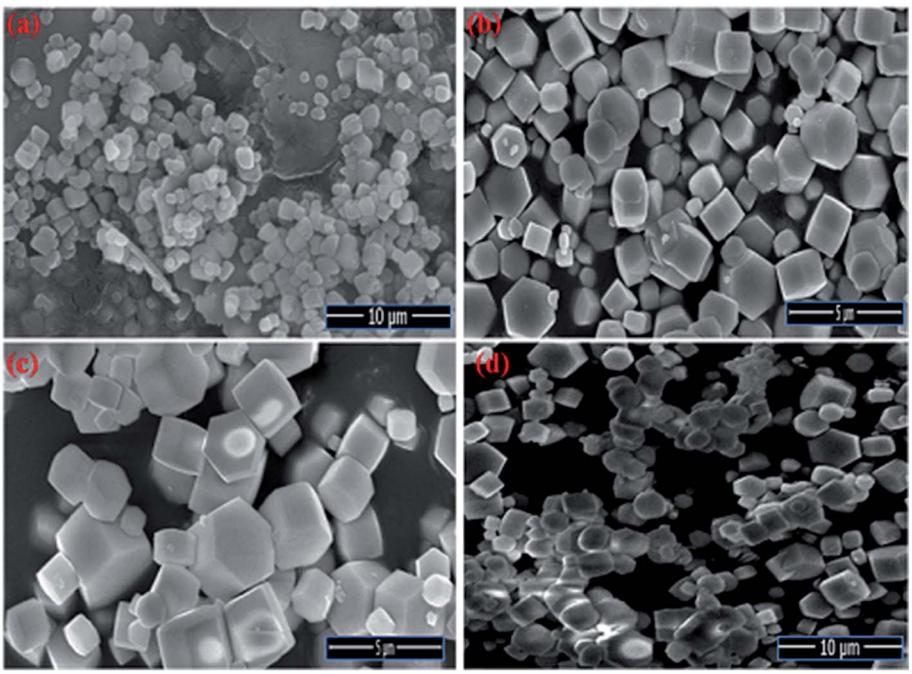


Fig. 4 FESEM micrographs depicting the variation in the morphology of nanophosphors from cubic to hexagonal $NaCeF_4$:$Tb^{3+}$ at different temperatures (a) 120 °C (b) 140 °C (c) 160 °C (d) 180 °C.

samples. The result obtained is tabulated in Tables S1 and S2: ESI.† The spatial distribution of elements involves Na, Ce, Tb, Eu, and F in the as-prepared $NaCeF_4$:$Tb^{3+}$ and $NaCeF_4$:$Tb^{3+}$/$Eu^{3+}$ nanophosphors. Furthermore, the presence of additional elements like N, O and C in the EDS spectrum validates the formation of PEI-functionalized nanoparticles. The presence of crucial element like C in the R-GO and R-GO@PEI@$NaCeF_4$:$Tb^{3+}$/$Eu^{3+}$ nanocomposite samples confirms the formation of carbon based R-GO and R-GO doped nanocomposite. The spectral peaks of samples computing the presence of Y, Ce, Gd, Eu, Tb, Na, C, N, O and F elements are shown in Fig. S2–S4: ESI.†

### Scanning electron microscopy and high-resolution transmission electron microscopy

The Field emission Scanning Electron Microscopy (FE-SEM) Transmission Electron Microscopy (TEM) and high-resolution Transmission Electron Microscopy (HR-TEM) analysis was utilized to monitor the shape, size and morphology of nanomaterials. Fig. 4 displays the FE-SEM micrographs of synthesized $NaCeF_4$:$Tb^{3+}$ at varying reaction parameters. The morphology of the nanophosphors was systematically tuned by heating temperature from 120 °C to 180 °C. During the growth mechanism, NaCeF4:$Tb^{3+}$ exhibited two different crystal morphologies and phase transformation occurred from kinetically stable cubic shape (α-phase) at 120 °C to thermodynamically stable hexagonal shape (β-phase) at around 160 °C.[51] It was observed from the micrographs that the 160 °C is a suitable temperature resulting in smooth-surfaced pure hexagonal-shaped nanoparticles. To further monitor the effect of $Eu^{3+}$ ions, as-synthesized $NaCeF_4$:$Tb^{3+}$/$Eu^{3+}$ aliquots were analyzed (with varying $Eu^{3+}$ contents from 1 to 7%) and results are shown in Fig. 5. The $Eu^{3+}$ ion concentration caused tunable effect on the morphology and size of the resultant nanoparticles architecture, ranging from smooth-surfaced 2D hexagonal plate-like morphology in the early stage (1–3%) to aggregated broad sized hexagonal rods at the later stage of the reaction bearing a higher concentration of $Eu^{3+}$ (7%). The overall result showed that$Eu^{3+}$ ion exhibits dual-mode character, showing active luminescent property and also notable morphological agent for the synthesized nanostructure reaction. Hence, the reaction temperatures as well as metal ion concentration emerge as important factors in adapting an improved morphology and shape of nanomaterial. Fig. S5: ESI† displays the TEM micrographs of $NaCeF_4$:$Tb^{3+}$/$Eu^{3+}$ showing hexagonal shape and PEI-$NaCeF_4$:$Tb^{3+}$/$Eu^{3+}$ confirming the presence of a aggregated layer-like structures on to the surface of PEI capped hexagonal nanophosphor.[52]

Furthermore, the FE-SEM and TEM micrographs of composites of R-GO with nanophosphor were also analyzed to explore the morphological effect of sheets like R-GO on the luminescent nanophosphor as shown in Fig. 6 and 7. The result noticed the transparent crumbled sheet like the layered structure of R-GO. Fig. 6(b) and 7(b) display the FE-SEM and TEM micrographs of the synthesized R-GO@PEI-$NaCeF_4$:$Tb^{3+}$/$Eu^{3+}$ nanocomposite depicting the exquisite doping of hexagonal-shaped PEI-$NaCeF_4$:$Tb^{3+}$/$Eu^{3+}$ nanoparticles onto the R-GO sheets.

The high-resolution transmission electron microscopy (HR-TEM) images confirm the high crystallinity of the prepared nanophosphors (see Fig. S6 and S7: ESI†). From the micrographs (shown in Fig. 8), it is indicated that the lattice fringe spacing between interlayer planes lies in the range of 0.27 nm to 0.3 nm, which is well indexed with the (101) lattice plane of the hexagonal

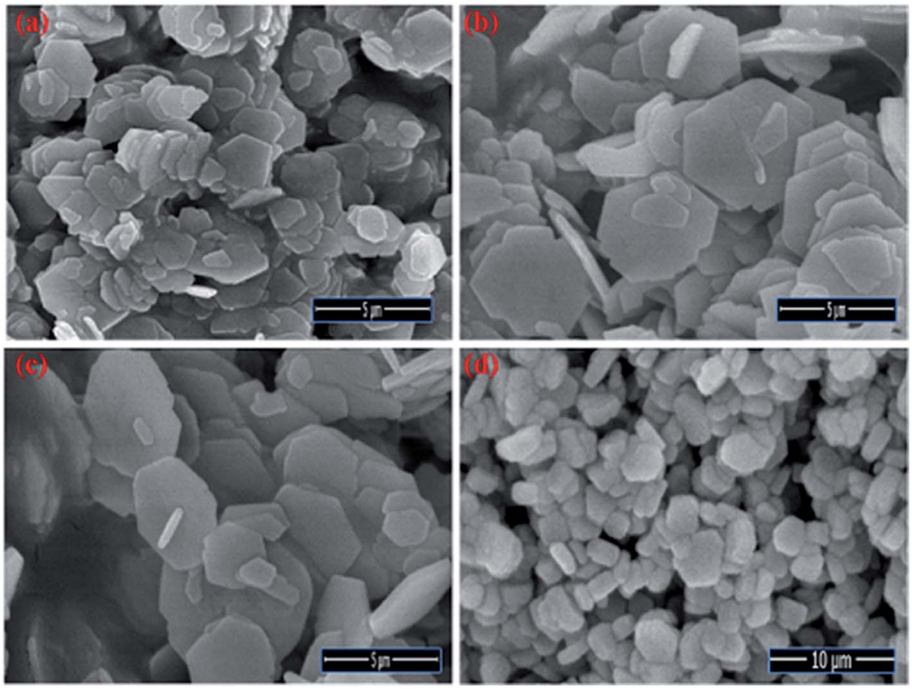


Fig. 5 FE-SEM images visualizing the morphological effect of $Eu^{3+}$ ion contents on the hexagonal $NaCeF_4$:$Tb^{3+}$/$Eu^{3+}$ nanophosphors (a) 1% (b) 3% (c) 5% (d) 7%.

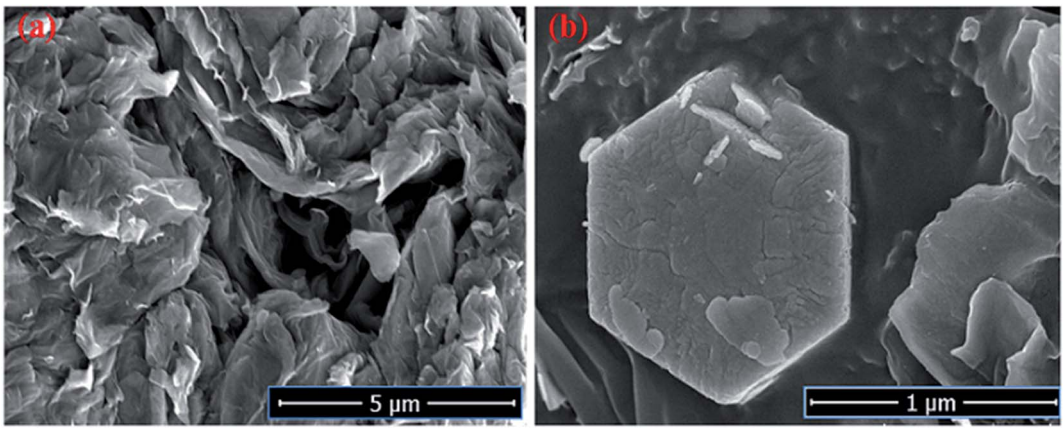


Fig. 6 FE-SEM micrographs of (a) R-GO (b) RGO@PEI@$NaCeF_4$:$Tb^{3+}$/$Eu^{3+}$ (Eu-7%) nanocomposite.

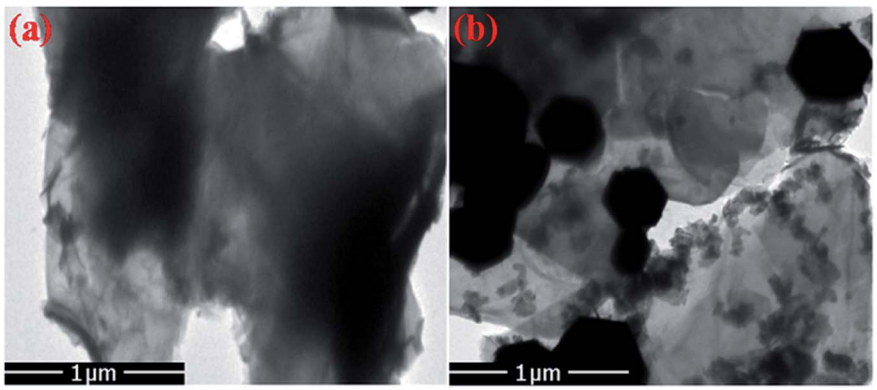


Fig. 7 TEM images of (a) R-GO (b) RGO@PEI@$NaCeF_4$:$Tb^{3+}$/$Eu^{3+}$ (Eu-7%) nanocomposite showing the presence of hexagonal nanoparticles anchored on the R-GO sheets.

$NaCeF_4$ structure.[53] The existence of ordered lattice fringes corresponding to the hexagonal phase is in good agreement with the results of the X-ray diffraction (XRD) patterns. The nanophosphors result in preferential growth orientation along the 002 direction.

### Infrared spectroscopy

FT-IR spectroscopy was used to explore the presence of functional groups in the synthesized $NaCeF_4$:$Tb^{3+}$/$Eu^{3+}$ nanocrystals as well as for the PEI functionalized $NaCeF_4$:$Tb^{3+}$/$Eu^{3+}$ nanophosphors as shown in Fig. S8: ESI.† The FT-IR spectra were selectively recorded within range of the wave number 4000–

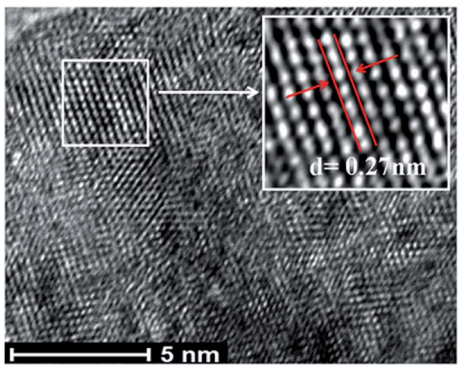


Fig. 8 HR-TEM micrograph showing PEI-functionalized $NaCeF_4$:-$Tb^{3+}$/$Eu^{3+}$ (Eu-7%) nanostructure.

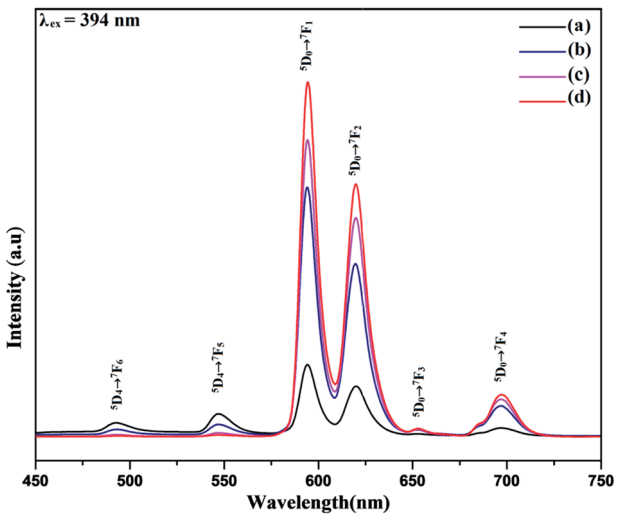


Fig. 9 Room-temperature photoluminescent emission spectra of $NaCeF_4$:$Tb^{3+}$/$Eu^{3+}$ displaying different emissions at varying $Eu^{3+}$ concentrations (a) 1% (b) 3% (c) 5% (d) 7%.

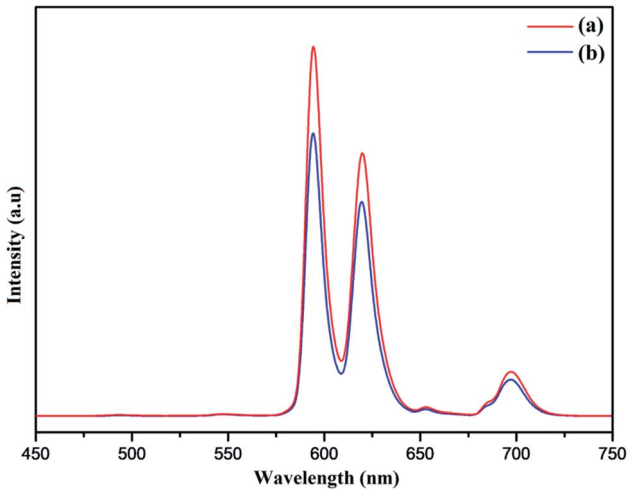


Fig. 10 Room-temperature photoluminescent emission spectra of (a) PEI-$NaCeF_4$:$Tb^{3+}$/$Eu^{3+}$ (Eu-7%) (b) $NaCeF_4$:$Tb^{3+}$/$Eu^{3+}$ (Eu-7%).

400 $cm^{-1}$. The IR spectra revealed intense broad absorption band at 3400 $cm^{-1}$ assigning to stretching vibration of the adsorbed –OH molecules on the surface of $NaCeF_4$:$Tb^{3+}$/$Eu^{3+}$ nanophosphors. The bands at 2924 and 2850 $cm^{-1}$ correspond to asymmetrical and symmetrical stretching vibration modes of the methylene group ($-CH_2$) respectively. The bands around 1640 and 1400 $cm^{-1}$ are attributed to asymmetrical and symmetrical stretching of the carboxylate (–COO) group.[54] The appearance of these IR bands confirms the presence of EDTA in the $NaCeF_4$:$Tb^{3+}$ and $NaCeF_4$:$Tb^{3+}$/$Eu^{3+}$ nanocrystals.

Meanwhile, to monitor the proper functionalization of PEI onto the surface of nanoparticles the FT-IR spectrum of the prepared sample was recorded and compared with that of pure $NaCeF_4$:$Tb^{3+}$/$Eu^{3+}$ nanocrystals fabricated without PEI Fig. S9: ESI.† The existence of PEI is confirmed by the presence of the characteristic absorption peaks at 3389 $cm^{-1}$ corresponds to N–H stretching vibration of the $NH_2$ group. The band around 1380–1630 $cm^{-1}$ is due to vibration of the amide group.[55] For the additional bonding with any external ligand, the presence of free amine groups on the surface of the nanoparticles is of extreme importance as these can bind with the outer molecules. The band at 1527 $cm^{-1}$ (Fig. S9: ESI†) corresponding to amine groups confirms the presence of free amine groups still vacant on the surface nanoparticles for further attachment.[56] An absorption band around 1391 $cm^{-1}$ is attributed to stretching vibrations of the C–N bond of amino acid (see Fig. S9: ESI†). Meanwhile, it was interesting to note that all the above bands were not observed in the pure EDTA capped

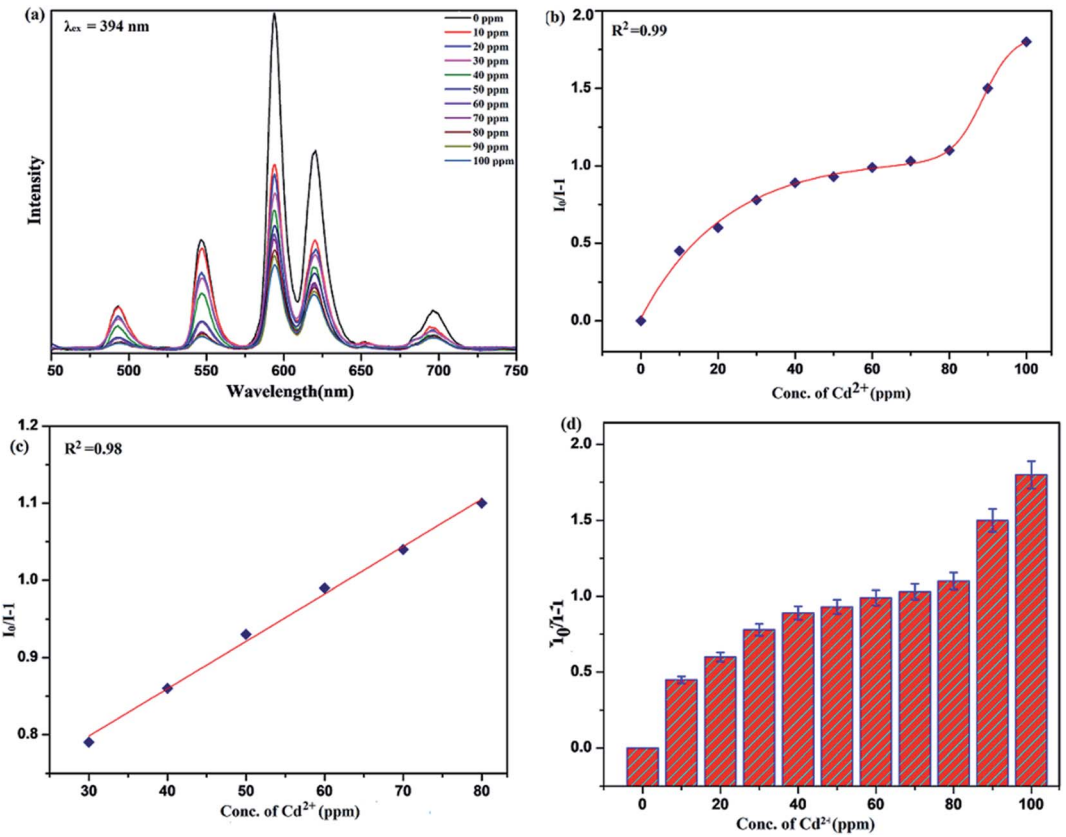


Fig. 11 Variation in photoluminescence intensity of nanosensor in presence of different $Cd^{2+}$ concentrations (from 0 to 100 ppm) selective excitation at $\lambda_{ex} = 394$ nm: (a) emission spectra of nanophosphors with addition of $Cd^{2+}$ ion (b) nonlinear Stern–Volmer plot of $I_0/I - 1$ *versus* ($Cd^{2+}$) concentrations (c) linear Stern–Volmer fitting and (d) error bar.

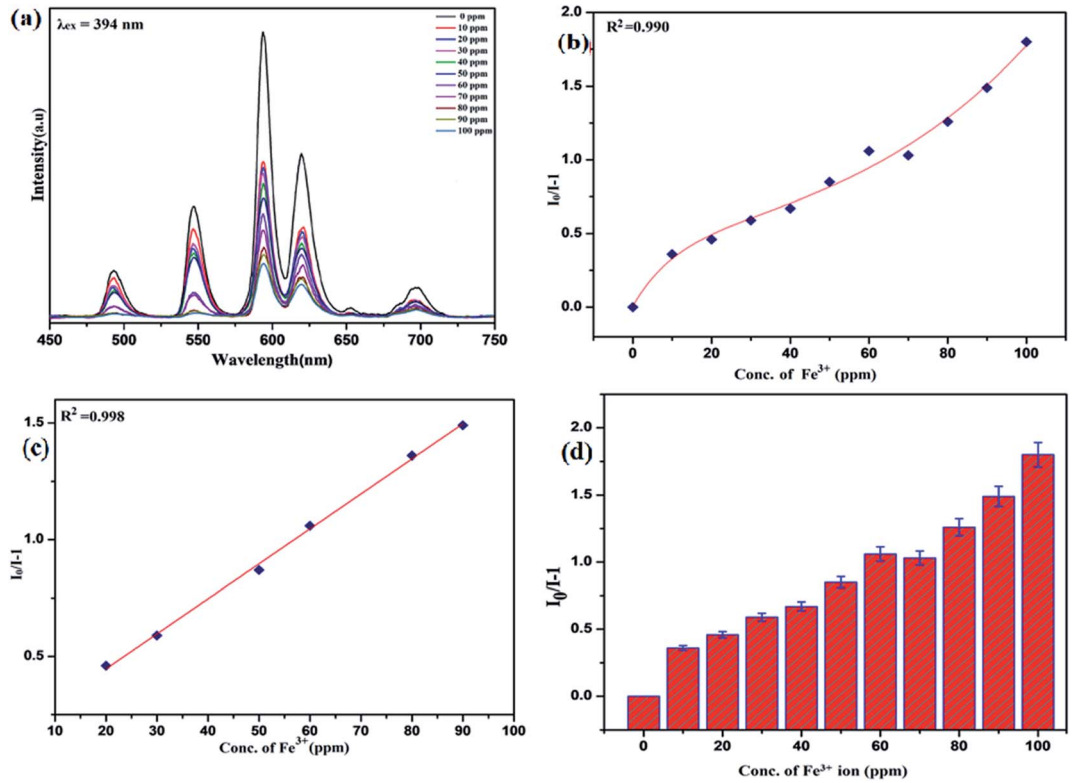


Fig. 12 Variation in photoluminescence intensity of nanosensor in presence of different $Fe^{3+}$ concentrations (from 0 to 100 ppm) selective excitation at $\lambda_{ex} = 394$ nm: (a) emission spectra of nanophosphors with addition of $Fe^{3+}$ ion (b) nonlinear Stern–Volmer plot of $I_0/I - 1$ *versus* ($Fe^{3+}$) concentrations (c) linear Stern–Volmer fitting and (d) error bar.

nanocrystals confirming the successful functionalization of PEI on to the nanophosphor.

Additionally, FT-IR spectrum was further recorded to investigate the presence of functional groups and bonding interaction of the GO, R-GO and the PEI-$NaCeF_4$:$Tb^{3+}$/$Eu^{3+}$@R-GO nanocomposite as depicted in Fig. S10: ESI.† The occurrence of characteristic peak at 3430 $cm^{-1}$ is attributed to the stretching vibration of hydroxyl groups (–OH) present on the GO sheets. The IR spectrum of GO demonstrates the presence of abundant oxygen containing functional moieties including C=O functional groups (band around 1734 $cm^{-1}$) and epoxy groups (asymmetric vibration at 1232 $cm^{-1}$).[57] There occurs a drastic change in the IR spectrum of R-GO where shift in bands is observed from 1628 $cm^{-1}$ to around 1586 $cm^{-1}$ due to the reduction process.[58] Fig. S11: ESI† displays the FT-IR spectrum of the fabricated PEI-$NaCeF_4$:$Tb^{3+}$/$Eu^{3+}$@R-GO nanocomposite confirming the successfully binding interaction of various functional moieties remaining on the R-GO sheets with the nanophosphor. The shift in the band positions confirms the sufficient anchoring of metal nanophosphor onto the R-GO layered structure.

## Photoluminescent properties

The photoluminescence spectra of the synthesized $Tb^{3+}$ doped $NaCeF_4$ nanostructures was monitored under single excitation wavelength 247 nm as shown in Fig. S12: ESI.† The emission peaks centred at 490, 545, 585 and 621 nm are corresponding to various transitions resulting from excited state $^5D_4$ to ground state $^7F_J$ ($J = 6, 5, 4, 3$) respectively. The presence of strong peak at 545 nm *i.e.*, $^5D_4 \rightarrow {}^7F_5$ originates due to the magnetic-dipole and electric-dipole allowed transition.[59] The emission from $Tb^{3+}$ is sensitized by $Ce^{3+}$.

The photoluminescence spectra of $NaCeF_4$:$Tb^{3+}$/$Eu^{3+}$ nanophosphors with varying $Eu^{3+}$ concentrations (1%, 3%, 5% and 7%) were also recorded to investigate the luminescence behaviour and effect of different $Eu^{3+}$ ion concentrations on the PL intensity as displayed in Fig. 9. The $Ce^{3+}$ ion (having 4f–5d allowed transition) can also sensitize $Eu^{3+}$ ion which can act as an activator and improve the luminescence competency of the nanophosphors.[60] However, direct sensitization of $Eu^{3+}$ from $Ce^{3+}$ is prohibited due to metal to metal electron charge transfer (MMCT) *i.e.*, $Ce^{3+} + Eu^{3+} \rightarrow Ce^{4+} + Eu^{2+}$ resulting in abrupt fall off photoluminescence intensity.[61] $Tb^{3+}$ ion (green-emitter) can be employed as bridging material for improved energy transfer from the $Ce^{3+}$ ion to $Eu^{3+}$ ion with minimum quenching effect. The results observed indicate effective energy transfer with superior luminescence emission.[62] Thus, apart from being an efficient activator, $Tb^{3+}$ can also be employed as a competent mediator between the sensitizer ($Ce^{3+}$) and activator ($Eu^{3+}$) resulting in minimizing the MMCT quenching.[63] Consequently, there occur well-built green orange emissions under ultraviolet excitation occurring due to energy transfer (ET) from $Ce^{3+} \rightarrow Tb^{3+}$ and $Tb^{3+} \rightarrow Eu^{3+}$.

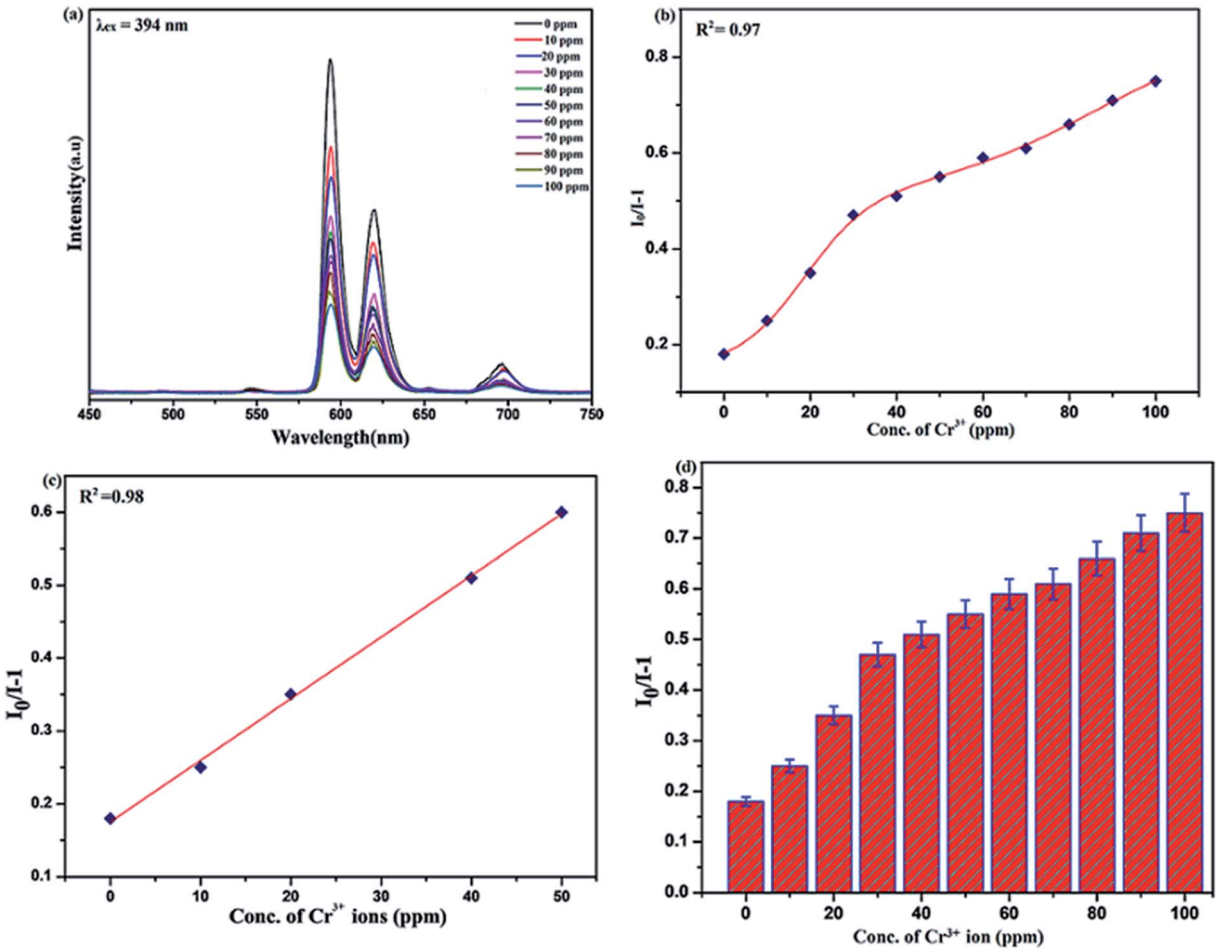


Fig. 13 Variation in photoluminescence intensity of nanosensor in presence of different $Cr^{3+}$ concentrations (from 0 to 100 ppm) selective excitation at $\lambda_{ex} = 394$ nm (a) emission spectra of nanophosphors with addition of $Cr^{3+}$ ion (b) nonlinear Stern–Volmer plot of $I_0/I - 1$ *versus* ($Cr^{3+}$) concentrations (c) linear Stern–Volmer fitting and (d) error bar.

The Photoluminescence spectra of the $NaCeF_4$:$Tb^{3+}$/$Eu^{3+}$ with different $Eu^{3+}$ concentrations displayed in Fig. 9 reveal the existence of four characteristics emission peaks (under 394 nm excitation) arising from different transitions centered at 594 ($^5D_0 \rightarrow {}^7F_1$), 624 ($^5D_0 \rightarrow {}^7F_2$), 657 ($^5D_0 \rightarrow {}^7F_3$), 700 ($^5D_0 \rightarrow {}^7F_4$). The peak centered at 657 nm ($^5D_0 \rightarrow {}^7F_3$) and 700 nm ($^5D_0 \rightarrow {}^7F_4$) may be due to magnetic and electric-dipole forbidden transitions of $NaCeF_4$:$Tb^{3+}$/$Eu^{3+}$ nanophosphors.[64] The PL intensity varies with the change in $Eu^{3+}$ ion concentrations. The PL spectrum (Fig. 9) shows an enhancement in the luminescence intensity with the increase in the $Eu^{3+}$ concentrations ranging from 1% to 7% as displayed. From the graph it is observed that sample having $Eu^{3+}$ ion 7% content achieved maximum luminescence intensity showing efficient energy transfer to the $Eu^{3+}$ ion. It is quite interesting to note that the peaks occurring at 493 and 548 nm correspond to the characteristic emission peaks of $Tb^{3+}$. The decrease in the $Tb^{3+}$ peaks with increase in the $Eu^{3+}$ concentration manifest the effective energy transfer from $Tb^{3+}$ to $Eu^{3+}$ ions as shown in Fig. 9.

Furthermore, the PL spectrum of the PEI functionalized nanophosphor was also investigated showing improved photoluminescence intensity of the nanophosphor as depicted in Fig. 10. The PL emission spectrum shows an enhancement in the emission intensity as compared to the $NaCeF_4$:$Tb^{3+}$/$Eu^{3+}$ nanophosphor. In order to investigate the energy transfer process in the nanophosphor the life time decay curve was measured. The lifetime of $NaCeF_4$:$Tb^{3+}$ and $NaCeF_4$:$Tb^{3+}$/$Eu^{3+}$ nanocrystals were recorded by taking into consideration the excitation and emission wavelength at 394 and 610 nm respectively (see Fig. S13 and S14: ESI†). The luminescence decay curves $NaCeF_4$:$Tb^{3+}$/$Eu^{3+}$ are in good agreement with the single exponential function $I = I_0 + A\exp(t/\tau)$ (where $I$ and $I_0$ are luminescence intensities at the time '$t$' and '0', the term $\tau$ stands for photoluminescence decay time). The lifetimes of $NaCeF_4$:$Tb^{3+}$ measured are in the range of 125 ms to 128 ms while the lifetimes of the $Eu^{3+}$ doped $NaCeF_4$:$Tb^{3+}$ (at different $Eu^{3+}$ concentrations) and PEI functionalized $NaCeF_4$:$Tb^{3+}$/$Eu^{3+}$ varies from 131 ms to 138 ms. The $NaCeF_4$:$Tb^{3+}$/$Eu^{3+}$ exhibit much longer lifetime as compared to the $Tb^{3+}$ doped nanophosphors suggesting an

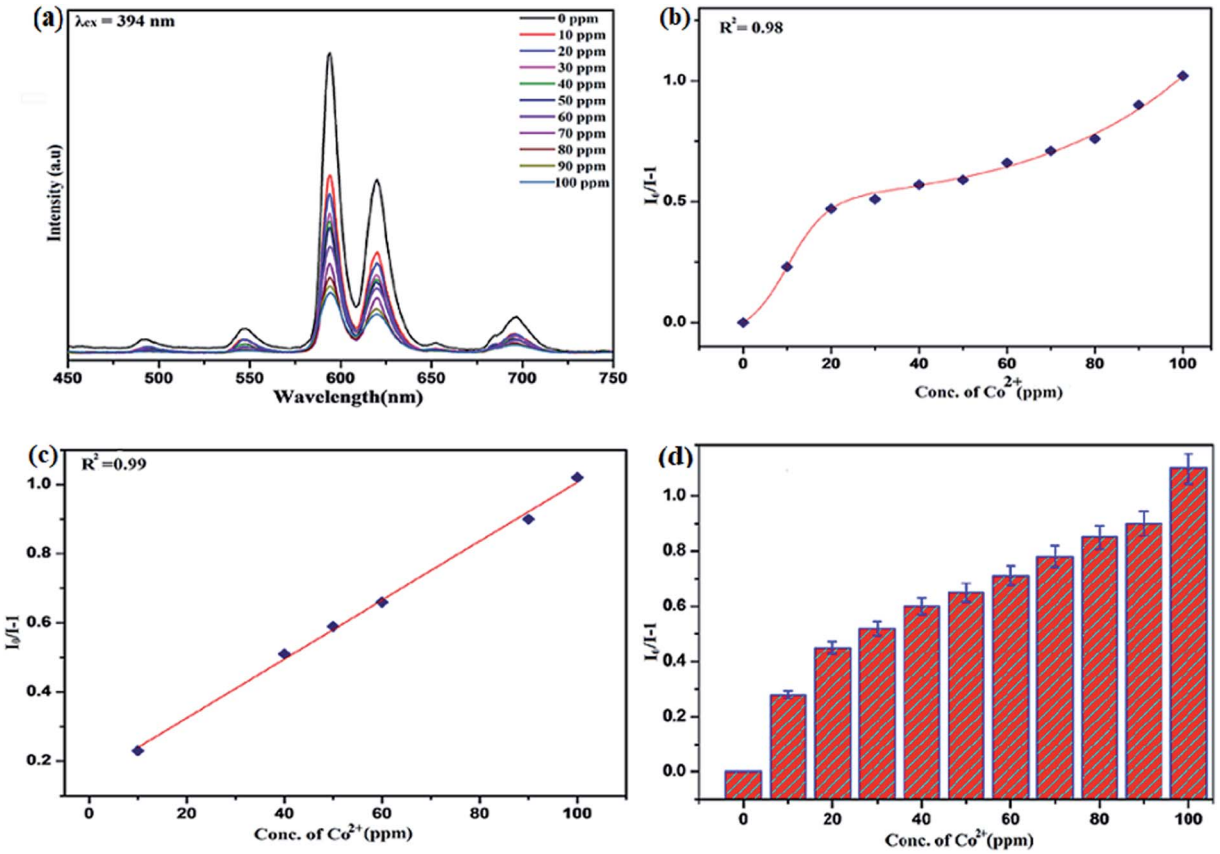


Fig. 14 Variation in photoluminescence intensity of nanosensor in presence of different $Co^{2+}$ concentrations (from 0 to 100 ppm) selective excitation at $\lambda_{ex} = 394$ nm (a) emission spectra of nanophosphors with addition of $Co^{2+}$ ion (b) nonlinear Stern–Volmer plot of $I_0/I - 1$ *versus* ($Co^{2+}$) concentrations (c) linear Stern–Volmer fitting and (d) error bar.

improved energy transfer process between the adjacent metals ions.

### Luminescent behavior and sensing properties

Lanthanide-doped nanocrystals due to their unique luminescence properties (such as their excellent chemical stability, narrow bandwidth emission, photo stability, tunable emission color) turn out promising candidates for luminescent based materials.[65] The photoluminescent spectra of synthesized PEI functionalized $NaCeF_4$:$Tb^{3+}$/$Eu^{3+}$ nanophosphor was explored for the fluorescence detection of toxic metal ions and hazardous nitro-aromatics compounds. It has been systematically demonstrated that PEI-functionalized $NaCeF_4$:$Tb^{3+}$/$Eu^{3+}$ nanophosphor can easily and efficiently sense the aromatic nitro compounds as well as toxic heavy metal ions even at trace level. All the photo luminescent spectra were recorded at room temperature using water as the dispersion medium. As shown in Fig. 10, PEI capped $NaCeF_4$:$Tb^{3+}$/$Eu^{3+}$ nanophosphor displays a sharp emission peak centered at 594 and 624 nm under $\lambda_{ex} =$ 394 nm when dispersed in water.

### Sensing of toxic heavy metal ions

To unfold the fluorescence sensing ability of the synthesized nanophosphor utilized for the detection of toxic heavy metal ions ($Cd^{2+}$, $Fe^{3+}$, $Cr^{3+}$, $Co^{2+}$) a series of luminescence-based experiments were performed. Equal amounts of the metals ions were added to the dispersed solution of nanophosphor. The suspension was taken in a 4 mm cuvette for luminescence measurement and compared with the luminescence intensity of the bare sample without the addition of analytes. Similar experiments were performed with other metal ions. The results demonstrated that the luminescence emission intensity of nanophosphor gets significantly influenced with the addition of different metal analytes bearing different concentrations ranging from 0 to 100 ppm. It was observed that the PL intensity is significantly quenched by the addition of metals ions and results obtained are displayed in Fig. 11 to 14 (for various metals analytes). The detection mechanism was strictly based on the interaction of the lone pair of $NH_2$ group present on the surface of nanophosphor with the metals ions leading to charge transfer from the electron rich nanophosphor material to the vacant metal ions resulting in luminescence quenching and ultimate metal sensing. Meanwhile, it was observed that 100 ppm solution of metal ion completely quenched the luminescence intensity of the nanophosphor.

The gradual increased luminescence quenching with increase in the concentration of analytes was analyzed by using the Stern–Volmer (SV) equation.[66]

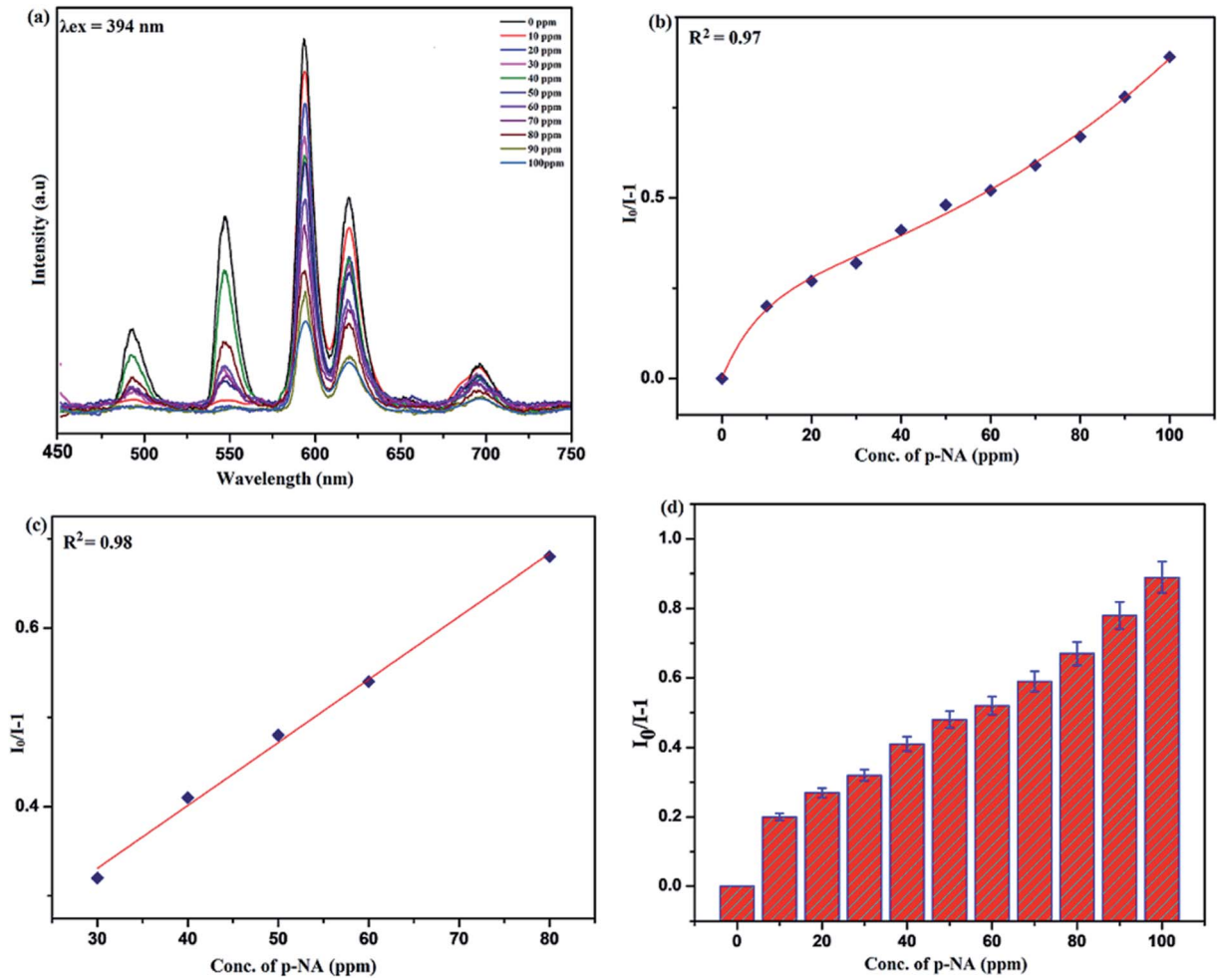


Fig. 15 Variation in photoluminescence intensity of nanosensor in presence of different *p*-NA concentrations (from 0 to 100 ppm) selective excitation at $\lambda_{ex} = 394$ nm: (a) emission spectra of nanophosphors with addition of p-NA (b) nonlinear Stern–Volmer plot of $I_0/I - 1$ *versus* (*p*-NA) concentrations (c) linear Stern–Volmer fitting and (d) error bar.

$$I_0/I = 1 + K_{SV}[Q]$$

$$K_{SV} = k_q\tau_f$$

Here, $I_0$ is the luminescence intensity in the absence of analytes, and $I$ is the luminescence intensity in the presence of metals ions, $Q$ is the concentration of analytes and $K_{SV}$ is the Stern–Volmer (SV) quenching constant, $k_q$ is the bimolecular quenching rate constant and $\tau_f$ is radiative life time. The affinity between PEI-functionalized nanophosphor (Eu-7%) and analytes (heavy metal ions and aromatic nitro-compounds) corresponding to $K_{SV}$ follows the order $Fe^{3+} > Cr^{3+} > Co^{2+} > Cd^{2+}$. The calculated $K_{SV}$ values for $Fe^{3+}$, $Cr^{3+}$, $Co^{2+}$, $Cd^{2+}$ are $3.8 \times 10^4$ $M^{-1}$, $2.6 \times 10^4$ $M^{-1}$, $1.8 \times 10^4$ $M^{-1}$, $0.85 \times 10^4$ $M^{-1}$ respectively. The $Fe^{3+}$ ions exhibited highest $K_{SV}$ value as compared to other metals ions which suggest high selectivity of the PEI-functionalized $NaCeF_4$:$Tb^{3+}$/$Eu^{3+}$ (Eu-7%) nanophosphors for $Fe^{3+}$ ion. The quenching efficiency for investigated heavy metal ions is found in a range of 73 to 90.02% (see Fig. S13: ESI†).

### Sensing of nitro-aromatic compounds

Benefiting from the above sensing properties of fabricated nanophosphor which could significantly quench the emission in aqueous media, the ability of this nanoprobe was again investigated to sense harmful nitro aromatics at even very low concentration. Similar detection experiment were performed considering selected toxic aromatic nitro compounds like picric acid (PA), *para*-nitrophenol (*p*-NP) *para*-nitroaniline (*p*-NA), and 4-nitrotoluene (4-NT). The photoluminescence results clearly indicate the selective and sensitive detection of nitro analytes by PEI-functionalized $NaCeF_4$:$Tb^{3+}$/$Eu^{3+}$ nanophosphor at trace level. The sensing principle is purely based on the charge transfer from the lone pairs of the amine group present on the nanophosphor with the electron deficient aromatic nitro compounds. This electronic interaction between the electron rich and electron deficient moieties leads to photoluminescence quenching. The effect of these different moieties on photo physical properties of nanophosphor was studied, by analyzing the emission spectra of PEI-functionalized compound in

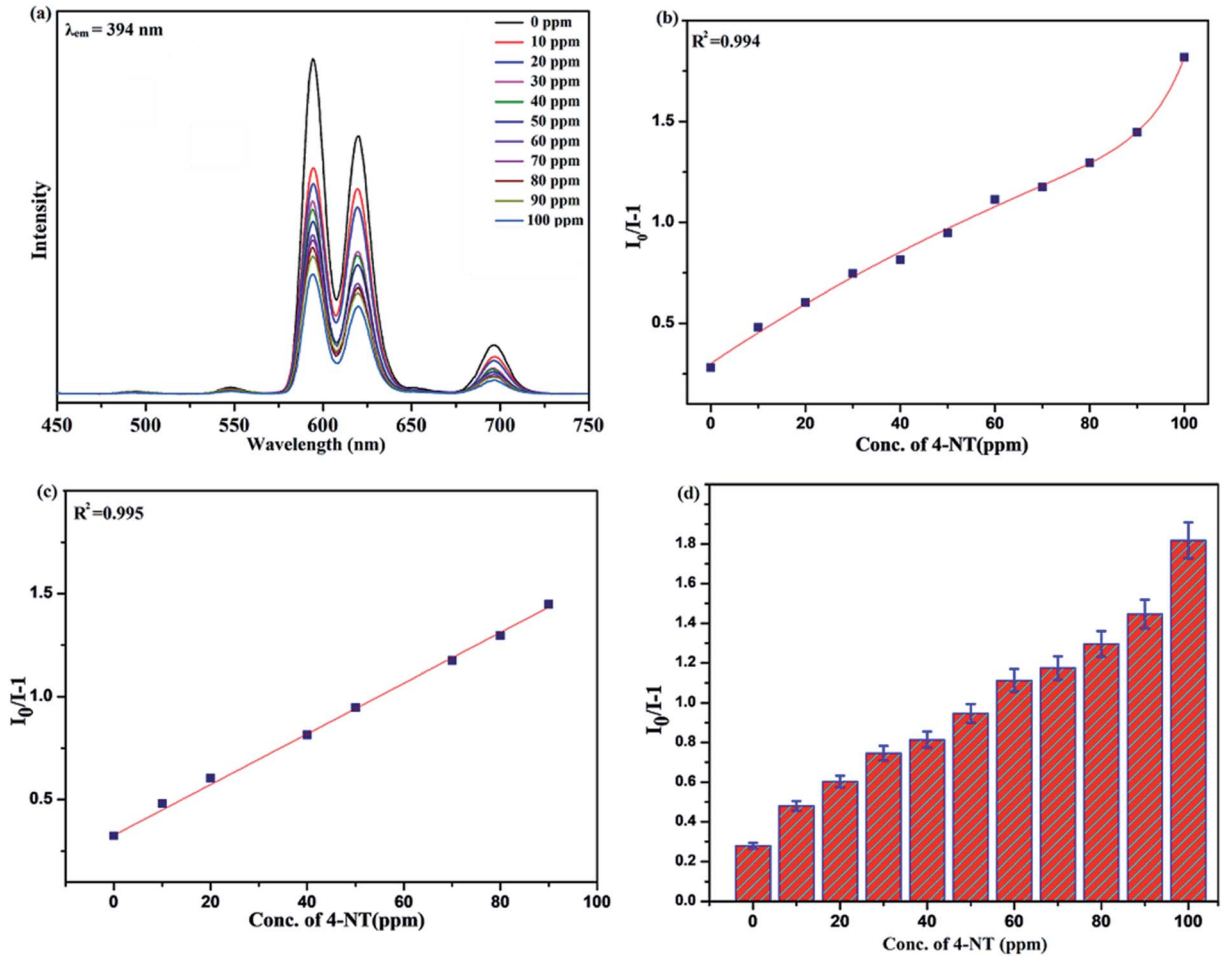


Fig. 16 Variation in photoluminescence intensity of nanosensor in presence of different 4-NT concentrations (from 0 to 100 ppm) selective excitation at $\lambda_{ex} = 394$ nm (a) emission spectra of nanophosphors with addition of 4-NT (b) nonlinear Stern–Volmer plot of $I_0/I - 1$ *versus* (4-NT) concentrations (c) linear Stern–Volmer fitting and (d) error bar.

distilled water excited at 394 nm in presence of varying concentrations of analytes. It was interestingly noticed that the luminescent intensity of the nanophosphor was significantly affected by addition of various concentration of aromatic nitro-compound ranging from 0 to 100 ppm. The experiments were also performed under similar conditions with $NaCeF_4$:$Tb^{3+}$/$Eu^{3+}$ (Eu-7%) nanophosphor without PEI functionalization. The results showed subdued response of luminescence intensity of nanophosphor in presence of analytes. Furthermore, nitro compounds lead to significant quenching of the luminescence intensity of the PEI functionalized nanophosphor and the results obtained are displayed in Figs. 15 to 18 (for different nitro analytes). It is again observed that for 100 ppm solution of picric acid the quenching efficiency is about 97.05%. Thus, when compared with the other nitro analyte solutions, picric acid causes maximum quenching of the luminescence intensity as depicted in Fig. S14: ESI.† Consequently, it can be postulated that the PEI-functionalized $Tb^{3+}$/$Eu^{3+}$ co-doped $NaCeF_4$ nanophosphor can act as an effective chemo sensors for the sensing of ultra trace amount of harmful picric acid analyte in aqueous solution. The calculated $K_{SV}$ of nitrocompounds follow the order PA ($2.25 \times 10^5$ $M^{-1}$) > *p*-NP ($1.8 \times 10^5$ $M^{-1}$) > *p*-NA ($1.1 \times 10^5$ $M^{-1}$) > 4-NT ($0.88 \times 10^5$ $M^{-1}$). The high $K_{SV}$ value for PA suggest the high selectivity of synthesized nanocrystals towards PA. Consequently, it was concluded that the $K_{SV}$ of $Fe^{3+}$ and PA is quite high as compared to other analyte compounds suggesting superior selectivity of the chemosensor for $Fe^{3+}$ and PA.

By using linear regression method detection limit (LOD) for the sensing of different analytes were calculated using formula $3\sigma/S$ where 3 denotes the 95% confidence level factor; $S$ is the slope of linear calibration curve and $\sigma$ is the standard deviation of the observed intensity for the blank PEI-functionalized $NaCeF_4$:$Tb^{3+}$/$Eu^{3+}$ (Eu-7%) nanostructure. The LOD for different aromatic nitrocompounds and heavy metal ions are as follow: 1.32 ppm (PA), 2.88 ppm (*P*-NP), 4.24 ppm (*P*-NA), 5.59 ppm (4-NT), 1.39 ppm ($Fe^{3+}$), 2.58 ppm ($Cr^{3+}$), 3.85 ppm ($Co^{2+}$) and 7.48 ppm ($Cd^{2+}$) respectively. The PA and Fe exhibit low detection limit as compare to that of other analytes and thereby suggested high sensitivity of the nanoprobe. As shown in Tables 1 and 2, the corresponding

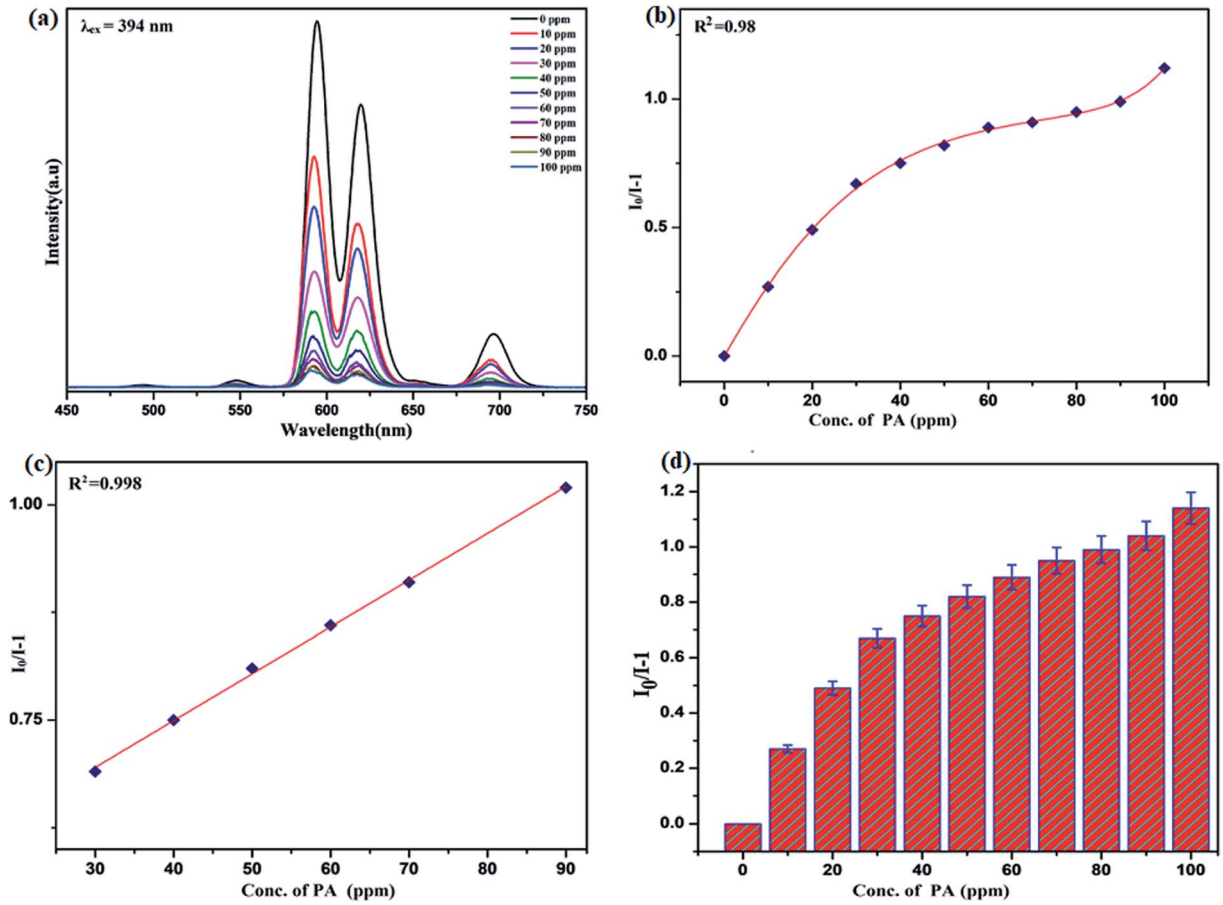


Fig. 17 Variation in photoluminescence intensity of nanosensor in presence of different PA concentrations (from 0 to 100 ppm) selective excitation at $\lambda_{ex} = 394$ nm: (a) emission spectra of nanophosphors with addition of PA (b) nonlinear Stern–Volmer plot of $I_0/I - 1$ *versus* (PA) concentrations (c) linear Stern–Volmer fitting and (d) error bar.

$K_{SV}$ and LOD of PA and Fe is higher than those of some previously reported.[67–76]

### Quenching mechanism of metal ions and nitro-aromatic analytes

The possible quenching mechanism for the detection of analytes is based on the donor–acceptor interaction between PEI-functionalized $NaCeF_4$:$Tb^{3+}$/$Eu^{3+}$ (Eu-7%) nanophosphor with different concentrations of analytes (nitroaromatics and heavy metal ions). The electron deficient nitro groups on the nitro aromatics interact with the lone pairs of the amine group present on the nanophosphor. Consequently, charge transfer takes place between the electron donor and electron acceptor group resulting in formation of stable acid–base Jackson Meisenheimer complex having negative charge delocalized over the ring of nitro analytes.[77] The stable σ-complex so formed consequently leads to luminescence quenching due to energy transfer from luminescence nanophosphor to analyte.[78] The incessant decrease in the luminescence intensity induces ultimate detection of the nitroaromatic analytes. For the detection of heavy metal ions similar donor–acceptor charge transfer mechanism is considered to account for the luminescence quenching effect.[79] The charge transfer occurs from the electron rich PEI functionalized nanophosphor having lone pair of electrons to the electron deficient metals ions having vacant orbitals. The charge migration between the luminophore to the acceptor result in the quenching of luminescence intensity and ultimate detection of heavy metal ions by the PEI doped nanophosphor. The above results thus, specify PEI functionalized nanophosphor as a good candidate for the exquisite detection of nitro aromatics as well as for the heavy metals ions.

### Photoluminescence spectra of R-GO@PEI@$NaCeF_4$:$Tb^{3+}$/$Eu^{3+}$ nanocomposite

Additionally, to unravel the impact of reduced graphene oxide on photoluminescence behavior and quenching phenomenon of the nanophosphor, the composites of R-GO and nanophosphor was investigated. Firstly, the photoluminescence spectrum of the RGO@$NaCeF_4$:$Tb^{3+}$/$Eu^{3+}$ was recorded at room temperature at excitation wavelength of 394 nm as shown in Fig. 19. Complete quenching of luminescence of the nanocomposite was observed due to the strong quenching effect of

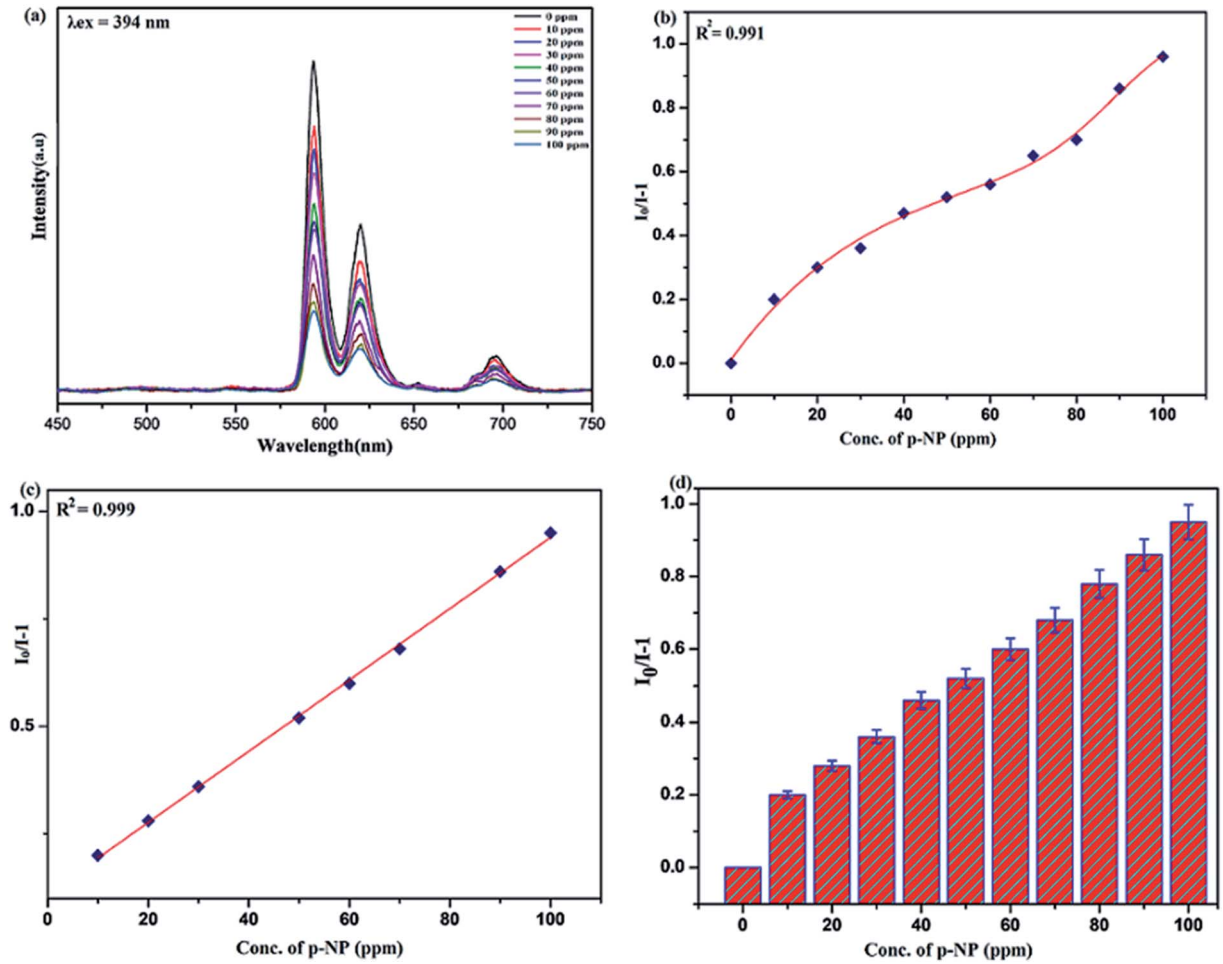


Fig. 18 Variation in photoluminescence intensity of nanosensor in presence of different *p*-NP concentrations (from 0 to 100 ppm) selective excitation at $\lambda_{ex} = 394$ nm: (a) emission spectra of nanophosphors with addition of *p*-NP (b) nonlinear Stern–Volmer plot of $I_0/I - 1$ *versus* (*p*-NP) concentrations (c) linear Stern–Volmer fitting and (d) error bar.

Table 1 Detection of nitroaromatic compounds by various methods from different nanomaterials

| Sensing method | Materials | Detection of NACs | $K_{SV}$ ($M^{-1}$) | LOD | Reference |
|---|---|---|---|---|---|
| Electrochemical method | $Cu_2O$ | PA | — | 39 μM | 67 |
| Electrochemical method | Nano-gold/glassy carbon | NP | — | 8 μM | 68 |
| Electrochemical method | AuBFE | PA | — | 13.1 μM | 69 |
| Fluorescence method | TPE-CMPs | 2,4-DNT | $1.84 \times 10^3$ | — | 70 |
| | | 2,6-DNT | $1.70 \times 10^3$ | | |
| | | TNP | $1.19 \times 10^4$ | | |
| Fluorescence method | Tb-MOFs | PA | $7.47 \times 10^4$ | — | 71 |
| Fluorescence method | FIrPicOMPBHCz | PA | $1.9 \times 10^4$ | 10 μM | 72 |
| | | *p*-NP | $5.6 \times 10^3$ | 44 μM | |
| | | DNP | $9.1 \times 10^3$ | 13 μM | |
| | | DNT | $1.2 \times 10^3$ | 44 μM | |
| | | NP | $5.6 \times 10^3$ | 44 μM | |
| | | NBA | $2.1 \times 10^3$ | 25 μM | |
| Fluorescence method | $[CH_3\text{-dpb}]2[Mg_3(1,4\text{-NDC})4(\mu\ H_2O)2(CH_3OH)(H_2O)]\cdot 1.5H_2O$ | PA | $2.8 \times 10^4$ | — | 73 |
| | | 2,4-DNA | $0.8 \times 10^4$ | — | |
| Fluorescence method | Serine-functionalised $NaYF_4$:$Ce^{3+}$/$Gd^{3+}$/$Eu^{3+}$@$NaGdF_4$:$Tb^{3+}$ | PA | $4.364 \times 10^4$ | 1.67 ppm | 40 |
| | | *p*-NP | $1.337 \times 10^4$ | 4.57 ppm | |
| | | *p*-NT | $0.824 \times 10^4$ | 6.36 ppm | |
| Fluorescence method | PEI-functionalised $NaCeF_4$:$Tb^{3+}$//$Eu^{3+}$ | PA | $2.25 \times 10^5$ $M^{-1}$ | 1.32 ppm | Present work |
| | | *p*-NP | $1.8 \times 10^5$ $M^{-1}$ | 2.88 ppm | |
| | | *p*-NA | $1.1 \times 10^5$ $M^{-1}$ | 4.24 ppm | |
| | | *p*-NT | $0.88 \times 10^5$ $M^{-1}$ | 5.59 ppm | |

Table 2 Detection of heavy metal ions by various methods from different nanomaterials

| Sensing method | Materials | Detection of heavy metal ions | $K_{SV}$ ($M^{-1}$) | LOD | Reference |
|---|---|---|---|---|---|
| Electrochemical method | RGO/$NiWO_4$ nanocomposite | $Cd^{2+}$ | — | $1.11 \times 10^{-10}$ M | 74 |
| | | $Pb^{2+}$ | | $2.04 \times 10^{-10}$ M | |
| | | $Cu^{2+}$ | | $2.80 \times 10^{-10}$ M | |
| | | $Hg^{2+}$ | | $3.05 \times 10^{-10}$ M | |
| Fluorescence method | $[(CH_3)_2NH_2]\cdot[Tb(bptc)]$ | $Fe^{3+}$ | — | 76.7 ppm | 75 |
| Fluorescence method | $[CH_3\text{-dpb}]2[Mg_3(1,4\text{-NDC})4(\mu\ H_2O)2(CH_3OH)(H_2O)]\cdot 1.5H_2O$ | $Fe^{3+}$ | $1.12 \times 10^4$ | — | 73 |
| | | $Cr^{3+}$ | $0.15 \times 10^4$ | — | |
| Fluorescence method | Water-soluble graphene oxide (GO) | $Fe^{2+}$ | $5.6 \times 10^3$ | — | 76 |
| | | $Hg^{2+}$ | $2.1 \times 10^3$ | | |
| Fluorescence method | PEI-functionalised $NaCeF_4$:$Tb^{3+}$//$Eu^{3+}$ | $Fe^{3+}$ | $3.8 \times 10^4$ | 1.39 ppm | Present work |
| | | $Cr^{3+}$ | $2.6 \times 10^4$ | 2.58 ppm | |
| | | $Cd^{2+}$ | $1.8 \times 10^4$ | 3.85 ppm | |
| | | $Co^{2+}$ | $0.88 \times 10^4$ | 7.48 ppm | |

reduced graphene oxide.[80] Interestingly, the PL spectrum of RGO@PEI@$NaCeF_4$:$Tb^{3+}$/$Eu^{3+}$ (Eu-7%) functionalized nanocomposite was recorded at excitation wavelength of 394 nm. It was interestingly observed that PL intensity of the nanophosphor recovers in the functionalized nanocomposite which was earlier quenched. The recovery of the PL intensity may be due to the presence of the PEI ligand which was capped around the nanophosphor surface. The PEI acts as bridging ligand which interconnects reduced graphene oxide and nanophosphor core. It was inferred that the PEI functionalized luminescent nanophosphor does not directly communicate with the graphene oxide. The quenching process taking place in the pure nanophosphor can be explained because of the direct interaction of core material with the RGO sheets leading to energy transfer and ultimate quenching of the PL in nanophosphor. On the other hand in the functionalized nanocomposite the PEI@$NaCeF_4$:$Tb^{3+}$/$Eu^{3+}$ (Eu-7%) complex is anchored on the RGO *via* the electrostatic interaction as well as hydrogen bonding between the $NH_2$ group of PEI and the functional moieties of RGO. This interaction keeps the core materials at far distance from the oxygen functionalizing group and thus reducing the quenching effect.[81] It may be assumed that firstly, there occur strong direct interactions between oxygen functionality of RGO and core materials leading to quenching of the luminescence intensity. However, when the PEI was used as the additional ligand, the $NH_2$ group present on the PEI molecule strongly interacts with the different functional moieties present on the negatively charged RGO sheets thus weakening the interaction between core materials and ultimately inhibiting quenching leading to recovery of the PL in nanophosphor.

In conclusion, the self assembly of the nanophosphor with the RGO not only achieves recovery in the photoluminescence intensity but there occur red PL emission from the $NaCeF_4$:$Tb^{3+}$/$Eu^{3+}$ as shown in Fig. 19. The red emission of the nanocomposite was confirmed by the presence of highly intense peak at 624 nm occurring due to transition from $^5D_0 \rightarrow {}^7F_2$ responsible for red emission in the PL spectrum.[82] Thus, culminated that the binding of PEI as capping agent not only minimizes the quenching of luminescence intensity of nanophosphor but also results in the red emission of the luminescence nanocomposite providing it as a novel candidate for emerging applications as optical sensors.

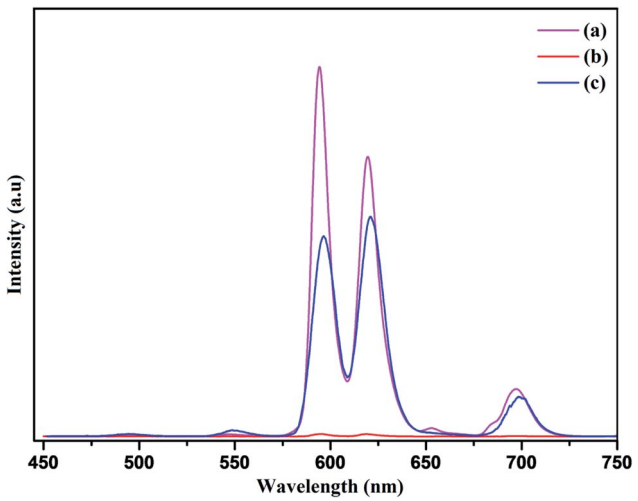


Fig. 19 Photoluminescence emission spectra of (a) $NaCeF_4$:$Tb^{3+}$/$Eu^{3+}$ (Eu-7%) nanophosphor (b) R-GO@$NaCeF_4$:$Tb^{3+}$/$Eu^{3+}$ (Eu-7%) (c) R-GO@ PEI@$NaCeF_4$:$Tb^{3+}$/$Eu^{3+}$ (Eu-7%).

## Conclusions

In summary, we have elaborately designed a highly selective and rapid luminescence nanosensor that can effectively detect the toxic analytes in the waste water. The presence of amine groups on the surface of PEI functionalized $NaCeF_4$:$Tb^{3+}$/$Eu^{3+}$ nanostructure enhance the efficiency of the detection of heavy metal ions and nitroaromatic compounds extensively. Additionally, with increased amounts of heavy metal ions and nitroaromatics, the luminescence emission of the fabricated nanoparticles is exponentially quenched. The quenching efficiency for the $Fe^{3+}$ ion and PA are found to be 90.02% and 97.05% respectively. Furthermore, $K_{SV}$ follows the order of ($Fe^{3+}$ > $Cr^{3+}$ >

$Co^{2+}$ > $Cd^{2+}$ with highest $K_{SV}$ value for $Fe^{3+}$) and for aromatic nitro compound as (PA > *p*-NP > *p*-NA > 4-NT). The data suggests high selectivity of novel PEI functionalized$NaCeF_4$:$Tb^{3+}$/$Eu^{3+}$ nanophosphor for the detection of $Fe^{3+}$ and picric acid (PA).

## Author contributions

Richa Singhaal: conceptualization, formal analysis, investigation & writing original draft. Lobzang Tashi: methodology and writing. Zaib ul Nisa: data curation & writing. Nargis Akhter Ashashi: software, review & editing. Charanjeet Sen and Swaita Devi: resources & validation. Haq Nawaz Sheikh: project administration & supervision.

## Conflicts of interest

The authors declare no competing financial interest.

## Acknowledgements

We acknowledge financial support from DST-PURSE-2 for photoluminescence facility. R. S acknowledges the support from Council of Scientific and Industrial Research New Delhi India (reference no. 09/100(0233)/2019-EMR-I) for JRF Fellowship. The authors also acknowledge the support from Advanced Material Research Centre (AMRC), IIT Mandi for FE-SEM analysis, Sophisticated Analytical Instrumentation Facility (SAIF), IIT Bombay for TEM and HR-TEM analysis and Sophisticated Analytical Instrumentation Facility (SAIF) Panjab University for PXRD and EDS.

## References

1 C. Li, Z. Hou, Y. Dai, D. Yang, Z. Cheng and J. Lin, *Biomater*, 2013, **1**, 213–223.
2 D. Wang, T. Xie and Y. Li, *Nano Res.*, 2009, **2**, 30–46.
3 G. Wang, Q. Peng and Y. Li, *Acc. Chem. Res.*, 2011, **44**, 322–332.
4 W. Abbas, I. Ahmad, M. Kanwal, G. Murtaza, I. Ali, M. A. Khan, M. N. Akhtar and M. Ahmad, *J. Magn. Magn. Mater.*, 2015, **374**, 187–191.
5 G. Chen, T. Y. Ohulchanskyy, S. Liu, W. C. Law, F. Wu, M. T. Swihart, H. Ågren and P. N. Prasad, *ACS Nano*, 2012, **6**, 2969–2977.
6 L. Tashi, M. Kumar, Z. Nisa, N. Nelofar and H. N. Sheikh, *New J. Chem.*, 2020, **44**, 1009–1020.
7 S. Sarkar, M. Chatti, V. NKB Adusumalli and V. Mahalingam, *ACS Appl. Mater. Interfaces*, 2015, **7**, 25702–25708.
8 R. Tu, B. Liu, Z. Wang, D. Gao, F. Wang, Q. Fang and Z. Zhang, *Anal. Chem.*, 2008, **80**, 3458–3465.
9 A. Efligenir, S. Déon, P. Fievet, C. Druart, N. M. Crini and G. Crini, *Chem. Eng. J.*, 2014, **258**, 309–319.
10 Y. Guan, C. Shao and M. Ju, *Int. J. Environ. Res. Public Health*, 2014, **11**, 7286–7303.
11 Y. Zou, X. Wang, A. Khan, P. Wang, Y. Liu, A. Alsaedi, T. Hayat and X. Wang, *Environ. Sci. Technol.*, 2016, **50**, 7290–7304.
12 A. Sepúlveda, M. Schluep, F. G. Renaud, M. Streicher, R. Kuehr, C. Hagelüken and A. C. Gerecke, *Environ. Impact Assess. Rev.*, 2010, **30**, 28–41.
13 H. K. Vardhan, P. S. Kumar and R. C. Panda, *J. Mol. Liq.*, 2019, **290**, 111197.
14 A. B. Lansdown, *Met Ions Life Sci*, 2011, **8**, 187–246.
15 S. Lambert and M. Wagner, *Chem. Soc. Rev.*, 2017, **46**, 6855–6871.
16 J. S. Becker, U. Breuer, H. F. Hsieh, T. Osterholt, U. Kumtabtim, B. Wu, A. Matusch, J. A. Caruso and Z. Qin, *Anal. Chem.*, 2010, **82**, 9528–9533.
17 Y. Lei, F. Zhang, P. Guan, P. Guo and G. Wang, *New J. Chem.*, 2020, **44**, 14299–14305.
18 J. Akhoundzadeh, M. Chamsaz, S. R. Yazdinezhad and M. H. Arbaz-zavvar, *Anal. Methods*, 2013, **5**, 778–783.
19 M. Najarro, M. E. D. Morris, M. E. Staymates, z. R. Fletcher and G. Gillen, *Analyst*, 2012, **137**, 2614–2622.
20 I. Bruzas, W. Lum, Z. Gorunmez and L. Sagle, *Analyst*, 2018, **143**, 3990–4008.
21 B. C. Blount, K. E. Milgram, M. J. Silva, N. A. Malek, J. A. Reidy, L. L. Needham and J. W. Brock, *Anal. Chem.*, 2000, **72**, 4127–4134.
22 J. L. Bricks, A. Kovalchuk, C. Trieflinger, M. Nofz, M. Büschel, A. I. Tolmachev, J. Daub and K. Rurack, *J. Am. Chem. Soc.*, 2005, **127**, 13522–13529.
23 M. G. Skalnaya and A. V. Skalny, *Essential trace elements in human health: a physician's view*, Publishing House of Tomsk State University, Tomsk, 2018, p. 224.
24 E. Grunwald and E. Price, *J. Am. Chem. Soc.*, 1964, **86**, 4517–4525.
25 J. A. Young, *J. Chem. Edu.*, 2008, **85**, 492.
26 W. Feng and X. Liu, *Chem. Soc. Rev.*, 2009, **38**, 976–989.
27 W. Zheng, P. Huang, D. Tu, E. Ma, H. Zhu and X. Chen, *Chem. Soc. Rev.*, 2015, **44**, 1379–1415.
28 B. Huang, H. Dong, K. L. Wong, L. D. Sun and C. H. Yan, *J. Phys. Chem.*, 2016, **120**, 18858–18870.
29 J. Zhou, J. L. Leano, Z. Liu, D. Jinn, K. L. Wong, R. S. Liu and J. G. Bunzli, *Small*, 2018, **14**(1–29), 1801882.
30 D. Hudry, I. A. Howard, R. Popescu and D. Gerthsen, *Adv. Mater.*, 2019, **31**, 1900623.
31 X. Liu and D. Yuan, *Sci. Rep.*, 2015, **5**, 1–13.
32 R. Naccache, Q. Yu and J. A. Capobianco, *Adv. Opt. Mater.*, 2015, **3**, 482–509.
33 J. L. Mason, H. Hassan, J. E. Topolski, H. P. Hratchian and C. C. Jarrold, *Acc. Chem. Res.*, 2019, **52**, 3265–3273.
34 M. Runowski, A. Shyichuk, A. Tymiński, T. Grzyb, V. Lavín and S. Lis, *ACS Appl. Mater. Interface*, 2018, **10**, 17269–17279.
35 O. J. Sovers and T. Yoshioka, *J. Chem. Phys.*, 1969, **51**, 5330–5336.
36 H. E. Townley, *Curr. Nanosci.*, 2013, **9**, 686–691.
37 M. Runowski, A. Bartkowiak, M. Majewska, I. R. Martín and S. Lis, *J. Lumin.*, 2018, **201**, 104–109.
38 C. Yan, H. Zhao, D. F. Perepichka and F. Rosei, *Small*, 2016, **12**, 3888–3907.
39 M. Malik, P. Padhye and P. Poddar, *ACS Omega*, 2019, **4**, 4259–4268.

40 L. Tashi, R. Singhaal, M. Kumar and H. N. Sheikh, *New J. Chem.*, 2020, **44**, 19908–19923.
41 W. Abbas, N. Akhtar, Q. Liu, T. Li, I. Zada, L. Yao, R. Naz, W. Zang, M. E. Mazhan, D. Zhang, D. Ma and J. Gu, *Sens. Actuators, B*, 2019, **282**, 617–625.
42 A. S. Saleemi, M. Hafeez, A. Munawar, N. Akhtar, W. Abbas, M. E. Mazhar, Z. Shafiq, A. P. Davis and S. L. Lee, *J. Mater. Chem. C*, 2020, **8**, 12984–12992.
43 W. Abbas, Q. Liu, N. Akhtar, J. Ahmad, M. E. Mazhar, T. Li, I. Zada, L. Yao, R. Naz, M. Imtiaz, W. Zhang, A. Amjad, D. Zhang and J. Gu, *J. Electroanal. Chem.*, 2019, **853**, 113560–113598.
44 P. K. Sarkar, N. Polley, S. Chakrabarti, P. Lemmens and S. K. Pal, *ACS Sens*, 2016, **1**, 789–797.
45 L. Shahriary and A. A. Athawale, *Int. J. Energy Environ. Eng.*, 2014, **2**, 58–63.
46 S. Park, J. An, J. R. Potts, A. Velamakanni, S. Murali and R. S. Ruoff, *Carbon*, 2011, **49**, 3019–3023.
47 J. Ladol, H. Khajuria, R. Singh, V. Kumar and H. N. Sheikh, *J. Mater. Sci.: Mater. Electron.*, 2017, **28**, 11671–11681.
48 H. Lian, Y. Dai, D. Yang, Z. Cheng, C. Li, Z. Hou, M. Shang and J. Lin, *Nanoscale*, 2014, **6**, 9703–9712.
49 S. Calvin, S. X. Luo, C. C. Broadbridge, J. K. McGuinness, E. Anderson, A. Lehman, K. H. Wee, S. A. Morrison and L. K. Kurihara, *Appl. Phys. Lett.*, 2005, **87**, 233102.
50 K. Huang, M. Lei, Y. J. Wang, C. Liang, C. X. Ye, X. S. Zhao, Y. F. Li, R. Zhang, D. Y. Fan and Y. G. Wang, *Powder Diffr.*, 2014, **29**, 8–13.
51 X. Qu, H. K. Yang, G. Pan, J. W. Chung, B. K. Moon, B. C. Choi and J. H. Jeong, *Inorg. Chem.*, 2011, **50**, 3387–3393.
52 X. Lei, R. Li, D. Tu, X. Shang, Y. Liu, W. You, C. Sun, F. Zhang and X. Chen, *Chem. Sci.*, 2018, **9**, 4682–4688.
53 X. Zhong, X. Wang, G. Zhan, Y. Tang, Y. Yao, Z. Dong, L. Hou, H. Zhao, S. Zeng, J. Hu and L. Cheng, *Nano Lett.*, 2019, **19**, 8234–8244.
54 T. Ji, P. Fan, X. Li, Z. Mei, Y. Mao and Y. Tian, *RSC Adv.*, 2019, **9**, 10645–10650.
55 Y. C. Chen, Y. C. Wu, D. Y. Wang and T. M. Chen, *J. Mater. Chem. A*, 2012, **16**, 7961–7969.
56 H. Cai, X. An, J. Cui, J. Li, S. Wen, K. Li, M. Shen, L. Zheng, G. Zhang and X. Shi, *ACS Appl. Mater. Interfaces*, 2013, **5**, 1722–1731.
57 D. R. Dreyer, S. Park, C. W. Bielawski and R. S. Ruoff, *Chem. Soc. Rev.*, 2010, **39**, 228–240.
58 P. G. Ren, D. X. Yan, X. Ji, T. Chen and Z. M. Li, *Nanotechnology*, 2011, **22**, 55705.
59 X. Qu, H. K. Yang, G. Pan, J. W. Chung, B. K. Moon, B. C. Choi and J. H. Jeong, *Inorg. Chem.*, 2011, **50**, 3387–3393.
60 S. Fischer and T. Jüstel, *J. Lumin.*, 2020, **223**, 117232.
61 M. Shang, S. Liang, H. Lian and J. Lin, *Inorg. Chem.*, 2017, **56**, 6131–6140.
62 F. N. Sayed, V. Grover, S. V. Godbole and A. K. Tyagi, *RSC Adv.*, 2012, **2**, 1161–1167.
63 J. Huo, L. Dong, W. Lü, B. Shao and H. You, *Phys. Chem. Chem. Phys.*, 2017, **19**, 17314–17323.
64 H. Guan, G. Liu, J. Wang, X. Dong and W. Yu, *New J. Chem.*, 2014, **38**, 4901–4907.
65 S. Gai, C. Li, P. Yang and J. Lin, *Chem. Rev.*, 2014, **114**, 2343–2389.
66 Z. u. Nisa, L. Tashi, C. Sen, N. A. Ashashi, S. C. Sahoo and H. N. Sheikh, *New J. Chem.*, 2020, **44**, 8125–8137.
67 S. James, B. Chishti, S. A. Ansari, O. Y. Alothman, H. Fouad, Z. A. Ansari and S. G. Ansari, *J. Electron. Mater.*, 2018, **47**, 7505–7513.
68 L. Chu, L. Han and X. Zhang, *J. Appl. Electrochem.*, 2011, **41**, 687–694.
69 V. Prchal, V. Vyskocil and J. Barek, *J. Electroche. Soc.*, 2010, **164**, H316–H320.
70 H. Namgung, J. J. Lee, Y. J. Gwon and T. S. Lee, *RSC Adv.*, 2018, **8**, 34291–34296.
71 L. H. Cao, F. Shi, W. M. Zhang, S. Q. Zang and T. C. W. Mak, *Chem.–Eur. J.*, 2015, **21**, 15705–15712.
72 W. Dong, Q. Ma, Z. Ma, Q. Duan, X. Lü, N. Qiu and Z. Su, *Dyes Pigm.*, 2020, **172**, 107799.
73 Z. F. Wu, L. K. Gong and X. Y. Huang, *Inorg. Chem.*, 2017, **56**, 7397–7403.
74 R. Kumar, T. Bhuvana and A. Sharma, *RSC Adv.*, 2017, **7**, 42146–42158.
75 X. L. Zhao, D. Tian, Q. Gao, H. W. Sun, J. Xu and X. H. Bu, *Dalton Trans.*, 2016, **45**, 1040–1046.
76 D. Y. Wang, D. W. Wang, H. A. Chen, T. R. Chen, S. S. Li, Y. C. Yeh, T. R. Kuo, J. H. Liao, Y. C. Chang, W. T. Chen and S. H. Wu, *Carbon*, 2015, **82**, 24–30.
77 T. Das, A. Pramanik and D. Haldar, *Sci. Rep.*, 2017, **7**, 1–12.
78 S. Sarkar, L. G. Suárez, W. Verboom, V. Mahalingam and J. Huskens, *ChemNanoMat*, 2016, **2**, 805–809.
79 M. Li, H. Gou, I. A. Ogaidi and N. Wu, *ACS Sustain. Chem. Eng.*, 2013, **1**, 713–723.
80 M. C. Hsiao, S. H. Liao, M. Y. Yen, P. I. Liu, N. W. Pu, C. A. Wang and C. C. M. Ma, *ACS Appl. Mater. Interfaces*, 2010, **2**, 3092–3099.
81 X. Zhang, W. Zhang, Y. Li and C. Li, *Dyes Pigm.*, 2017, **140**, 150–156.
82 C. Li, Z. Quan, J. Yang, P. Yang and J. Lin, *Inorg. Chem.*, 2007, **46**, 6329–6337.